

# A novel active contour model for medical images via the Hessian matrix and eigenvalues



Kazim Hanbay <sup>a,\*</sup>, Muhammed Fatih Talu <sup>b</sup>

<sup>a</sup> Computer Engineering Department, Bingol University, 12000, Bingol, Turkey

<sup>b</sup> Computer Engineering Department, Inonu University, 44280, Malatya, Turkey

## ARTICLE INFO

### Article history:

Received 29 May 2017

Received in revised form 29 September 2017

Accepted 21 January 2018

Available online 10 February 2018

### Keywords:

Active contour

Segmentation

Medical images

Eigenanalysis

Hessian matrix

## ABSTRACT

This paper presents a new level set formulation for active contour models (ACM). We propose the idea of integrating the eigenvalue information of Hessian matrix into the level set function. By this new level set function, the principal curvature information of images is used to enhance the ability of segmenting boundary regions. The advantages of our model are as follows: firstly, the interior and exterior object boundaries can be segmented with the initial contour being anywhere in the input image. Secondly, this method can work with heterogeneous images. Thirdly, the proposed model can produce smooth and right boundaries of objects having vital importance in medical operations. Extensive experiments demonstrate that the proposed model can obtain better segmentation results.

© 2018 Elsevier Ltd. All rights reserved.

## 1. Introduction

The segmentation is one of the necessary image processing techniques receiving significant attention in various computer vision applications including object recognition and classification. Active Contour Model (ACM) is one of the most popular segmentation techniques. The major consideration of ACM is to evolve a closed curve in order to obtain the correct object boundaries. Depending on how object boundary is detected, the ACMs can be categorized into parametric [1–5] and geometric models [6–17]. Parametric active contours (or snake) are based on an energy minimization, while the geometric active contours based on the theory of curve evolution. In general, geometric active contour models are given in a level set formulation.

The original active contour model was firstly proposed by Kass et al. [1], in which a parametric representation of the contour was used. This model has been known as energy-minimizing curves or snakes. However, it has significant drawbacks such as: (i) it needs prior information of the object boundary, (ii) it is easily affected by noise in the input image, (iii) it has difficulties caused by intensity inhomogeneities. With the improvement of active contour methodology, a large number of active contour models have been proposed to overcome such drawbacks. To address some of the key problems in the original model, Cohen [2] has modified the external forces that push the curve to the boundaries. In this model, the curve behaves like a balloon which is inflated by an additional force. Moreover, the contour curve passes over discontinuous boundary and is stopped only if the boundary is strong. One of the most efficient parametric active contours models is the Gradient Vector Flow (GVF) approach [3,4]. Xu and Prince [4] have used an external field to enhance the convergence to weak and long boundary structures. Ren et al. [5] proposed a new parametric GVF model based on the augmented Lagrangian method. They reformulated GVF model as a convex optimization problem, and used an effective optimization scheme. Moreover,

\* Corresponding author.

E-mail addresses: [khanbay@bingol.edu.tr](mailto:khanbay@bingol.edu.tr) (K. Hanbay), [fatih.talu@inonu.edu.tr](mailto:fatih.talu@inonu.edu.tr) (M.F. Talu).

they adopted the multiresolution approach to reduce the computational cost. Li et al. [6] proposed a region-based ACM in a variational level set formulation to deal with intensity inhomogeneity. They defined a region-scalable fitting (RSF) energy functional. RSF energy functional contains a contour and two fitting functions. Fitting functions were used to approximate the image intensities on the two sides of the active contour curve. RSF model provides the use of intensity information in image regions at a specific scale, but it is known sensitive to initialization. Recently, Zhang et al. [7] developed a level set active contour model (LSACM) for medical image segmentation in the presence of intensity inhomogeneity. In this model, the inhomogeneous objects are modeled as Gaussian distributions of different variances and means. Their model defines a mapping from the input image domain to another domain. To map the input image into another domain, a sliding window method is utilized. Since the intensity distribution of inhomogeneous object is Gaussian, these objects are more easily segmented. Finally, maximum likelihood energy functional is defined on the image regions. This functional combines the level set function, the bias field and the piecewise constant function approximating the original image.

Different from parametric active contour models, geometric active contour models have been developed in the literature. In general, image gradients have been used in these models to detect the edges of objects. Caselles et al. [13] developed a geometric active contour method based on curve evolution. This model includes a comprehensive mathematical analysis. To evolve the contour curve in the direction of normal force, energy based function is used. The contour curve is stopped at the object boundary. In [14], geometric active contour was proposed by using level set formulation. In this work, they adopt level set methods to the problem of shape recovery. With this approach, complex shapes can be detected from given images. However, this approach cannot converge to the object boundary accurately for images having low contrast between the background and the objects. To overcome such drawbacks, the geodesic active contour (GAC) [15] was developed. The GAC model uses gradient computation to construct an Edge Stopping Function (ESF). Moreover, the GAC model allows to connect geometric active contours based on the theory of curve evolution and traditional snakes based on energy minimization. The GAC is usually sensitive to weak edges and noise. Holtzman-Gazit et al. [16] developed a variational model, which uses a function including a geodesic active contour (GAC) term and edge-based term. The developed level set includes a minimal variance term that measures the homogeneity inside and outside the object. A robust numerical algorithm for the proposed model was developed in order to accelerate its convergence. Li et al. [18] proposed a new variational level set formulation called Distance Regularized Level Set Evolution (DRLSE). The proposed level set formulation provides stable level set evolution and efficient numerical scheme. Zhang et al. [19] developed an ACM which is carried out with a novel level set formulation. This model is implemented with a different processing named Selective Binary and Gaussian Filtering Regularized Level Set (SBGFLS) model. The ACM with SBGFLS utilizes the statistical pixel information of object regions to constitute a region-based Signed Pressure Force (SPF) function. As an alternative to ACM with SBGFLS model, Talu [20] developed an online region-based active contour method named ORACM. The ORACM utilizes a user-defined active contour and then continuously updates it. Although the ACM with SBGFLS and ORACM methods have some significant benefits, they cannot produce smooth object boundaries, and this tends to undesired active contours.

All the above reviewed geometric active contour models generally use image gradient calculation to attract the contour curve toward object boundaries. Since direct-gradient-based models depend on edge information, they have poor convergence to discontinuous boundary and noise. These models can benefit from a balloon force function to shrink or expand the active contour. In order to achieve better segmentation performance, the initial active contour curve must be located near the object edges, especially when complex boundary and strong noise are presented in the image [21,22].

On the other hand, some of geometric models cannot detect the discrete and weak object boundaries. To avoid this drawback, the Chan-Vese (CV) model [8] finds the correct object boundary in a variational level set formulation with intensity information, and it does not use the gradient information in level set formulation. The level set formulation of the CV model uses a region based energy function, which is derived from the Mumford-Shah model [23]. However, the CV model has much convergence range, and it does not work well for images with intensity inhomogeneity. Inspired by the C-V model, different ACMs have been proposed and used in several image processing problems [24–26]. In [26], Zhang et al. presented robust region based ACM using local image statistics. These statistics are calculated using local image fitting energy (LIF). Moreover, Gaussian filtering for variational level set has been used to regularize the level set function. Paragios and Deriche [27] proposed a boundary and region-based model under a curve-based optimization function. The proposed model has been obtained by unifying boundary-based and region information as an improved GAC model. The objective function is optimized using a gradient-descent algorithm. To obtain accurate cell boundaries, Ersoy et al. [28] proposed a modified geodesic active contour model. In this model, the level set evolution is performed by using a new adaptive stopping function. In [29], an efficient level set based active contour model has been developed to integrate both region and boundary information. This model uses hybrid level set formulation based on region term and curvature term. Especially, the region term developed in the level set formulation has the important advantages over the CV model in dealing with medical images with low contrast [29].

Some of the ACM models use gradient information of the current level set as a speed-controlling function [30]. When the active contour moves through the object boundaries, its speed can slow down, and produces rough object boundaries. This process causes very high computational cost. Moreover, the gradient computation along the weak object boundaries may cause a problem since the value of gradient vector here is nearly zero.

In this paper, we propose a novel geometric active contour model based on the eigenvalue analysis of Hessian matrix. Hessian matrix and its eigenvalues have been used in segmentation and enhancement of medical images, especially in the case of vessel images, which have thin and long structures that are difficult to distinguish [31]. In particular, the shape Hessian

of the energy function has been used to compute fast descent directions, because it significantly reduces the computational cost [32]. One typical variation of the Hessian matrix is proposed by Wang et al. [33] in which the Hessian matrix is incorporated into the GVF model. In this way, the improved GVF model can converge to discontinuous edges and preserve weak edges. The ratio between eigenvalues of the Hessian matrix was used for detection of blood vessels by increasing contrast between background and foreground objects [34,35]. The key contributions of our model can be summarized as follows:

1. Hessian matrix of the image is utilized to construct an edge stopping function.
2. This model includes eigenvalue computation of image surface to obtain robust edge locations.
3. The proposed algorithm is commonly faster than the state-of-the-art ACM models.

For a better understanding of differences of accuracy and speed between ACMs, the extensive simulations on different image types such as retinal, liver, lung, and brain images have been performed.

The paper is organized as follows: Section 2 reviews traditional active contour models. Then the proposed active contour model is described in Section 3. Section 4 gives the results of the proposed model and compares them with similar models. Conclusion is given in Section 5.

## 2. The C-V and ACM with SBGFRLS models

### 2.1. The C-V model

Chan and Vese [8] developed the level set method which can be seen as a special case of the Mumford–Shah energy functional [23]. Let  $I(x) : \Omega \rightarrow \mathbb{R}$  be a gray level image with pixel location  $x$ , and  $C : [0, 1] \rightarrow \Omega$  parameterized planar curve. A global approach is designed to determine a contour  $C$  that separates the image  $I$  into two non-overlapping regions: outside of the contour as background and inside the contour as foreground. The aim of C-V model is to calculate a piecewise constant approximation  $(c_1, c_2)$  of image  $I$  that minimizes the following energy function,

$$E^{CV}(c_1, c_2, C) = \lambda_1 \int_{inside(C)} |I(x) - c_1|^2 dx + \lambda_2 \int_{outside(C)} |I(x) - c_2|^2 dx + \mu Length(C) \quad (1)$$

where  $\lambda_1, \lambda_2$  and  $\mu$  are positive constant parameters and usually both set to 1.  $\lambda_1$  and  $\lambda_2$  control the image data driven force inside and outside  $C$ .  $c_1$  and  $c_2$  are two constants which denote the average intensity of pixels inside and outside of the active contour. With the level set method, the contour  $C$  is expressed as the Lipschitz continuous function  $\phi$ ,

$$\begin{cases} C = \{x \in \Omega : \phi(x) = 0\} \\ inside(C) = \{x \in \Omega : \phi(x) > 0\} \\ outside(C) = \{x \in \Omega : \phi(x) < 0\} \end{cases} \quad (2)$$

Then, the energy function  $E^{CV}(c_1, c_2, C)$  is represented by the zero level set of the Lipschitz function  $\phi(x)$ . Thus, the energy  $E^{CV}(c_1, c_2, C)$  can be written as,

$$\begin{aligned} E^{CV}(c_1, c_2, \phi) &= \lambda_1 \int_{\Omega} |I(x) - c_1|^2 H(\phi(x)) dx + \lambda_2 \int_{\Omega} |I(x) - c_2|^2 (1 - H(\phi(x))) dx \\ &\quad + \mu \int_{\Omega} \delta(\phi(x)) |\nabla \phi(x)| dx \end{aligned} \quad (3)$$

where  $H(\phi)$  and  $\delta(x)$  are Heaviside function and Dirac function, respectively. Generally, the Heaviside and the Dirac functions are selected as,

$$\begin{cases} H_{\varepsilon}(z) = \frac{1}{2} \left( 1 + \frac{2}{\pi} \arctan \left( \frac{z}{\varepsilon} \right) \right), z \in R \\ \delta_{\varepsilon}(z) = \frac{1}{\pi} \frac{\varepsilon}{\varepsilon^2 + z^2} \end{cases} \quad (4)$$

By minimizing the energy function in terms of  $c_1$  and  $c_2$ , we calculate  $c_1$  and  $c_2$  parameters as follows,

$$c_1(\phi) = \frac{\int_{\Omega} I(x) H(\phi) dx}{\int_{\Omega} H(\phi) dx} \quad (5)$$

$$c_2(\phi) = \frac{\int_{\Omega} I(x) (1 - H(\phi)) dx}{\int_{\Omega} (1 - H(\phi)) dx} \quad (6)$$

Minimizing the energy function  $E^{CV}(c_1, c_2, \phi)$  with respect to the level set function  $\phi(x)$ , we obtain the gradient descent flow with a notation using the Dirac delta function. Parameterizing the descent direction by an artificial time  $t$ , the variational

level set formulation can be obtained as,

$$\frac{\partial \phi(x, t)}{\partial t} = \delta(\phi) \left[ \mu \operatorname{div} \left( \frac{\nabla \phi(x)}{|\nabla \phi(x)|} \right) - \lambda_1(I(x) - c_1)^2 + \lambda_2(I(x) - c_2)^2 \right] \quad (7)$$

The C-V model has achieved good segmentation performance for images with intensity homogeneity. However, this model still has significant limitations. Firstly, if the intensities with inside  $C$  or outside  $C$  are inhomogeneity, the parameters  $c_1$  and  $c_2$  cannot be calculated accurately. Secondly, it is heavily dependent on the placements of initial contours. Thus, this model may get different results on same image by using different initial contours.

## 2.2. The ACM with SBGFLRS model

Zhang et al. [19] developed a region-based ACM which can use a region-based signed pressure function. This model benefits from the superiority of the GAC and C-V methods. The ACM with SBGFLRS model utilizes a new level set formulation. It uses a Gaussian smoothing filter to adjust the binary level set function in each iteration. The ACM with SBGFLRS model is defined as,

$$\frac{\partial \phi}{\partial t} = \operatorname{spf}(I(x)) \alpha |\nabla \phi|, \quad x \in \Omega \quad (8)$$

where  $|\nabla \phi|$  is the gradient of the level set function.  $\alpha$  is a constant parameter and controls the speed of level set function.  $\operatorname{spf}(I(x))$  denotes a signed pressure function, which is defined [19] as,

$$\operatorname{spf}(I(x)) = \frac{I(x) - \frac{c_1+c_2}{2}}{\max(|I(x) - \frac{c_1+c_2}{2}|)} \quad (9)$$

where  $c_1$  and  $c_2$  are described in Eqs. (5) and (6), respectively.

The ACM with SBGFLRS model supports the local or global segmentation. It decreases the cost of expensive re-initialization of the conventional level set formulations. It is not a parameter free algorithm. Since the parameter  $\alpha$  has great impact on the segmentation result, this parameter must be regularized for each input image. The choice of the constant parameter in this model is difficult.

## 3. The proposed method

In this section we propose a novel active contour model based on Hessian matrix to segment the images. Different from traditional active contour models, differential geometry based active contour model using both the  $\operatorname{spf}$  function and eigenvalues are introduced.

### 3.1. Basic idea

Edge-based ACMs benefit from image gradients to extract correct object edges. Moreover, the level set formulations benefit from the conventional gradient computation to construct an edge stopping function. However, such a function which is based on the gradient does not work well when the object boundaries are not prominent. To overcome this drawback, Jin et al. [31] embedded Hessian matrix information into the region-based active contour method. This method uses Hessian-based multiscale filtering to enhance the medical image. The segmentation results for medical images show that Hessian matrix is suitable and robust for the extraction of vascular tree. In this paper, to enhance the segmentation performance of the current level set functions, the idea of integrating the Hessian matrix and eigenvalue computations into the level set function is suggested.

A conventional way to analyze the local intensity changes of an image  $I$  is to evaluate its Taylor expansion in the neighborhood of a point  $x_0$ . Taylor expansion is defined as,

$$I(x_0 + \delta x, \sigma) \approx I(x_0, \sigma) + \delta x^T \nabla I(x_0, \sigma) + \delta x^T \mathcal{H}(I(x_0, \sigma)) \delta x \quad (10)$$

where  $\nabla I(x_0, \sigma)$  and  $\mathcal{H}(I(x_0, \sigma))$  are the gradient and Hessian matrix, which are calculated in  $x_0$  at scale  $\sigma$ .

The first order derivatives can be calculated by using different convolution filters such as the Sobel and Prewitt operators [36]. Similarly, the second order derivative can be calculated by the Laplacian filter. In the past years, two basic filters have been used in the literature for edge detection [37–40]: maxima of the first derivative and zero crossings of the second derivative. The first order derivatives are efficient to determine the strongest object edges by looking for the minimum and maximum in the image gradients while the zero-crossings of the second order derivatives are efficient for localization of the object edges. Suppose we have an image and a slightly blurred step function  $f(x)$  that express it. If we calculate the first and second order derivatives of  $f(x)$  signal (with respect to  $x$ ), we obtain the different results. For a given threshold value, the error of edge localization is a function of the slope of the first derivative in the neighborhood of zero. As shown in Fig. 1, rising slope causes positive high value first derivative while falling slope causes negative high value first derivative [36]. Edges can be determined by high value first derivative values. These high value regions of a first order derivative to a line produce two lines [39]. Thus, a special mechanism for calculation of the area between regions

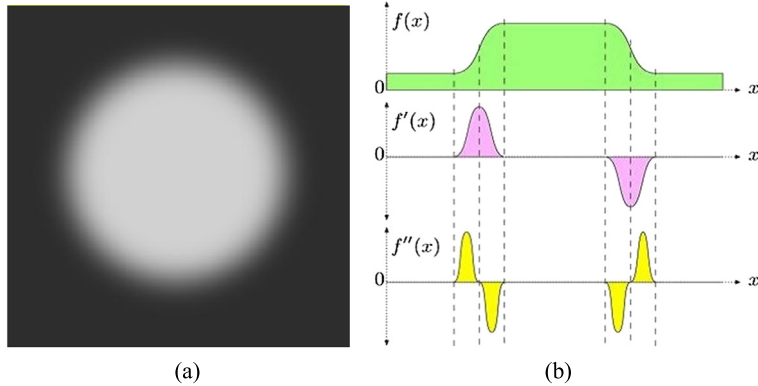


**Fig. 1.** A slightly blurred example image and blurred edge step function  $f(x)$ : (a) synthetic image, (b) the first and second order derivative results of edge step function  $f(x)$  [36].

is required. The edge operators based on first derivatives have some problems: (i) edge is proportional to pixel intensity transition, (ii) edges may be difficult to localize accurately, (iii) they produce thicker edges. From the viewpoint of second order derivatives, edges correspond to a zero crossing of the second order derivatives. Generally, the second order derivatives directly highlight regions of rapid intensity change without additional processing. Therefore, they are usually used as zero crossing edge detectors (see Fig. 1).

Similarly, the first and second order derivatives are analyzed in Fig. 2. For the 1D density function  $I$ , the first order derivative in any direction can be calculated with the gradient vector  $\nabla I$  and magnitude of the gradient  $|\nabla I|$ . The maximum gradient magnitude is the isotropic edge detector tool. This detector can find both the inner and outer edges of the object (Fig. 2a). It should be pointed that the performance of gradient operation can be enhanced using different kernel filters such as Gaussian filters. To minimize number of false edge points, the Canny operator at different scales achieves good localization of edges. Moreover, it behaves like the gradient using zero crossings of second derivative. However, our aim is not to identify which of the many first order derivative filters is the best one. In this paper, a level set model is proposed that allows to use second order derivatives.

In order to obtain an effective edge representation, we therefore consider the using of the second derivative filters on the boundary detection. The second order derivative is calculated through the Laplacian and Hessian operators. In second order derivative model, the neighborhood of a pixel for zero-crossing should be checked since the sign of second derivative changes. These operators have positive values at the outer regions and negative values at the inner regions of the objects (Fig. 2b). As a result, we use the Hessian approach for boundary detection instead of gradient-based edge detection. The proposed approach provides an equal filter response on both sides of an edge. Compared to the gradient magnitude operator, edge is represented by a smaller amount of pixels. Thus, we use this fact to extract the objects boundaries only by their internal side. It should be pointed that first derivatives are less sensitive to noise than the second derivatives. On the other hand, first derivatives can produce badly connected edges, while the second derivatives produce many zero crossings but also better connected edges. It should be noted the second order derivatives amplify image noise. To solve this issue, we use Gaussian smoothing filters.

In the literature, several methods at the calculation of second order derivatives have been used [31,35,38]. In two dimensions, the Gaussian first and second derivative filters are used to calculate the symmetric Hessian matrix. The readers are referred to [38] for the mechanism of computing the Hessian matrix of the input image. For a two dimensional image  $I(x, y)$ , the Hessian matrix is calculated as symmetric matrix of second order partial derivatives of image [41], and is defined as,

$$\mathcal{H}(x, y) = \begin{pmatrix} \frac{\partial^2}{\partial x^2} I(x, y) & \frac{\partial^2}{\partial x \partial y} I(x, y) \\ \frac{\partial^2}{\partial y \partial x} I(x, y) & \frac{\partial^2}{\partial y^2} I(x, y) \end{pmatrix} = \begin{bmatrix} D_{xx} & D_{xy} \\ D_{xy} & D_{yy} \end{bmatrix} \quad (11)$$

The eigenvalues of the Hessian matrix are calculated by solving the characteristic equation  $|\mathcal{H} - \lambda I| = 0$  for  $\lambda$  [41]. The eigenvalues are defined as,

$$\lambda_1 = \frac{1}{2} \left( D_{xx} + D_{yy} - \sqrt{-2D_{xx}D_{yy} + D_{xx}^2 + 4D_{xy}^2 + D_{yy}^2} \right) \quad (12)$$

$$\lambda_2 = \frac{1}{2} \left( D_{xx} + D_{yy} + \sqrt{-2D_{xx}D_{yy} + D_{xx}^2 + 4D_{xy}^2 + D_{yy}^2} \right) \quad (13)$$

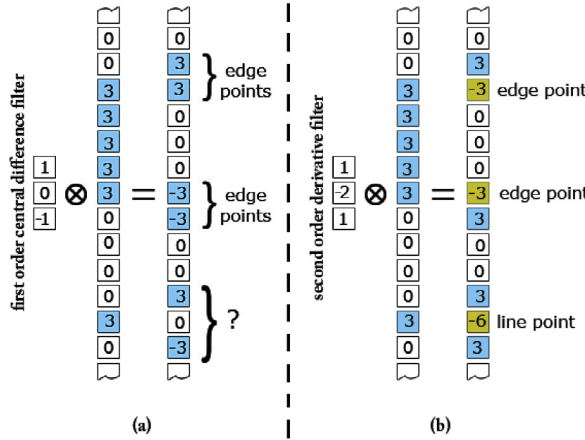


**Fig. 2.** Filter responses for the 1D pixel density: (a) responses of first order central difference filter; (b) responses of second order filter to an edge and to a line.

where  $\lambda_1$  and  $\lambda_2$  are the eigenvalues. They are called as the principal curvatures [38,41]. The product of the eigenvalues is equal to determinant of Hessian matrix. Since the eigenvalues contain the maximum amount of variance in object boundaries, eigenvalues of an image provide robust variation information among edge pixel points. These measurements are robust calculations for the likelihood of boundary pixels. Thus, we develop a novel level set function based on the eigenvalues as a measure for the edge detector. Fig. 3 shows the procedure for computing eigenvalues of the Hessian matrix at a specific Gaussian standard deviation.

### 3.2. The proposed level set function based on Hessian matrix

The aim of our model is to calculate a piecewise constant approximation  $(c_1, c_2)$  of image  $I$  that minimizes the following energy function,

$$E(c_1, c_2, C) = \int_{\text{inside}(C)} |I(x) - c_1| dx + \int_{\text{outside}(C)} |I(x) - c_2| dx, \quad x \in \Omega \quad (14)$$

where  $I(x) : \Omega \rightarrow \mathbb{R}$  and  $C : [0, 1] \rightarrow \Omega$  parameterized planar curve. The contour  $C$  that separates the image  $I$  into two non-overlapping regions: outside of the contour as background and inside the contour as foreground. With the level set method, the contour  $C$  is represented by the zero level set of the Lipschitz function  $\phi$  using Eq. (2). By minimizing the energy function in terms of  $c_1$  and  $c_2$ , we obtain  $c_1$  and  $c_2$  from Eqs. (5) and (6).

By incorporating the eigenvalues of Hessian matrix and *spf* function terms into Eq. (14) and optimizing them, we obtain the following energy function,

$$E(c_1, c_2, C) = \left( \int_{\text{inside}(C)} \frac{I(x) - \frac{c_1+c_2}{2}}{\max(|I(x) - \frac{c_1+c_2}{2}|)} dx + \int_{\text{outside}(C)} \left| \frac{I(x) - \frac{c_1+c_2}{2}}{\max(|I(x) - \frac{c_1+c_2}{2}|)} \right| dx \right) |\text{eig}(\mathcal{H}(I(x)))| \quad (15)$$

where  $|\text{eig}(\mathcal{H}(I(x)))|$  states the eigenvalue magnitude of Hessian of the image  $I(x)$ .

By keeping  $c_1$  and  $c_2$  fixed, we minimize the energy functional  $E(c_1, c_2, C)$  with respect to  $\phi$  to obtain the gradient descent flow as,

$$\frac{\partial \phi(x, t)}{\partial t} = H(\text{spf}(I(x))) \cdot |\text{eig}(\mathcal{H}(I(x)))| \quad (16)$$

where  $H(\phi)$  is the Heaviside function and  $\text{spf}(I(x))$  is the signed pressure function (SPF) described at Eq. (9). The size of magnitude matrix is equal to the  $I(x)$ . Magnitude of two eigenvalues can be calculated as,

$$u(x) = |\text{eig}(\mathcal{H}(I(x)))| = \sqrt{\lambda_1^2 + \lambda_2^2} \quad (17)$$

Eq. (16) includes two interesting terms: the first left term corresponds to the *spf* function, which can effectively extract object edges with the initial contour being anywhere in the noisy images. The second term in Eq. (16), which is related to the Hessian matrix of the image intensity along the principal directions, describes the change in pixel intensity. In addition, from the differential geometry point of view, the second term includes the principal curvature information of the object boundary regions. Moreover, the eigenvalues can minimize the curve length functional via the gradient descent algorithm. In contrast to the classical ACMs with the level set models, our model uses the Hessian matrix as the main part of the level

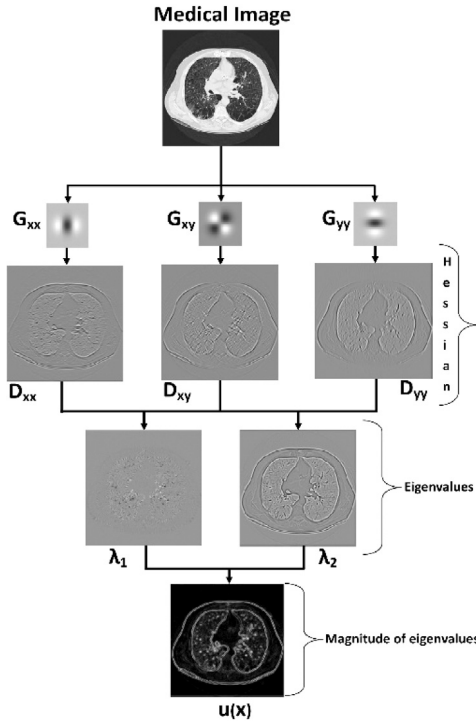


**Fig. 3.** Procedure for computing eigenvalues of the Hessian matrix. The Gaussian standard deviation  $\sigma = 1$ .

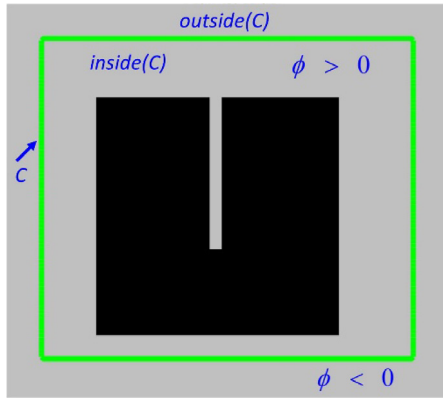


**Fig. 4.** Demonstration of the initial contour: *inside* ( $C$ ) and *outside* ( $C$ ) are zones inside and outside of contour, respectively.

set equation that plays a major role in reducing edge aliasing. An additional textural feature which is obtained from the eigenvalue analysis has the ability of driving the active contour into the thinner and weaker object boundaries. We observed that using only the eigenvalue components of the Hessian yields better boundary information than produced by the zero crossing of the Laplacian. The active contour curve evolves along the second-order derivative in the direction of the image eigenvalues.

The proposed model uses a user-defined active contour at the initialization stage of algorithm. The initialization of the contour is shown in Fig. 4. In our model, all of the objects are surrounded by the initial contour. After the initialization process, the contour rapidly starts evolving and finally segments an image into background and object regions. These parameters have different signs inside and outside of the active contour.

To regularize the level set function  $\phi$ , the level set models generally utilize the curvature-based regular function  $\text{div}(\nabla\phi/|\nabla\phi|)|\nabla\phi|$  [19]. Thus, we can rewrite the regularized term as  $\Delta\phi$ , which is the Laplacian of level set function  $\phi$ . Laplacian of the level set function  $\phi$  is equivalent to a Gaussian kernel filtering the initial condition of the level set function [19,42]. One of the hallmarks of the proposed model is the absence of the regular term  $\text{div}(\nabla\phi/|\nabla\phi|)|\nabla\phi|$ . Instead

of using the regular term, our proposed model uses a Gaussian filter to smooth the level set curve defining the segmented regions.

Moreover, the second order derivatives are more sensitive to noise than the first order derivative. The segmentation performance on noisy objects may become deteriorated. The Gaussian filter provides stable and smooth contour fitting. The standard deviation  $\sigma$  of the Gaussian filter is an important parameter. Thus it should be selected properly. If  $\sigma$  is too large, object boundaries may become blurred. On the other hand, if  $\sigma$  is too small, our model will be sensitive to noise. In our experiments, we use the Gaussian kernel as a  $K \times K$  filter mask.  $K$  is set to 5, and  $\sigma$  is set to 1. It is worth pointing out that, the above mentioned Gaussian filter is only used in level set evolution step. The application step of the Gaussian filter is presented in the following sections.

Based on these information, the proposed image segmentation method can measure the image sharpness and textural edge information. In the proposed model, eigenvalues are embedded into the level set function in order to overcome intensity inhomogeneity in adjacent regions and noise. Eigenvalues can suppress the noise effects besides providing important reduction in computation complexity. They are capable of preserving significant boundary structures while removing non-significant information. Frangi et al. [43] emphasize that eigenvalues have a significant role in the discrimination of the only local orientation pattern. They also present a geometric ratio based on the magnitude of eigenvalues. The geometric ratio only captures the local geometric information of image. It eliminates noise fluctuations and background pixels. To detect and eliminate noise, various methods using eigenvalues are proposed in the literature. For more details, readers may refer to [43–45].

The proposed model tries to address the problem of segmenting images with no training data. Furthermore, our model does not need any prior parameter. However, its smoothing process uses a parameter  $\sigma$ . In this paper, the parameter  $\sigma$  is empirically set to 1 for all experiments.

The main procedures of the proposed active contour model are described in the following iterative steps:

1. Initialize level set function  $\phi$  to be binary function as,

$$\phi(x, t=0) = \begin{cases} 1, & x \in \Omega_0 \\ -1, & x \in \Omega - \Omega_0 \end{cases} \quad (18)$$

where  $\Omega_0$  is a subset of the domain of image  $\Omega$  (see Fig. 4 in Section 3.1 for example).

2. Compute the Hessian matrix  $\mathcal{H}$  of the input image according to Eq. (11).
3. Compute the two eigenvalues  $\lambda_1$  and  $\lambda_2$  of the Hessian matrix according to Eq. (12) and Eq. (13).
4. Compute the eigenvalues magnitude  $u(x)$  according to Eq. (17).
5. Do the following iteration to solve the sub-problem:

- 5.1 While  $|\phi^{k+1} - \phi^k| > 0$ , ( $k$  is iteration number).
- 5.2 Compute  $c_1(\phi)$  and  $c_2(\phi)$  using Eq. (5) and Eq. (6).
- 5.3 Compute the  $spf$  function using Eq. (9).
- 5.4 Evolve the level set function using Eq. (16).
- 5.5 Update  $\phi(x)$  for the binary function as follows,

$$\phi(x) = \begin{cases} 1, & \phi(x) > 1 \\ -1 & \text{otherwise} \end{cases}$$

- 5.6 Apply a Gaussian filter to smooth the level set function.

6. End while, if the level set function has converged. If not, go to step 5.2.

### 3.3. Analytical discussion over the proposed model and ACM with SBGFLS model

The differences between proposed model and ACM with SBGFLS include the Hessian matrix and eigenvalue computation used in the proposed model. The ACM with SBGFLS model uses gradient computation to stop the contour evolution on the object edges. Local gradient information around object boundaries is used to regularize the level set function [46]. Once the local image gradient is calculated, there are several methods for obtaining object boundaries. For active contour problems, the ACM with SBGFLS uses the level set function as a penalty term. However, gradient computation is quite slow, and it depends on scaling. Because of using local gradient information, the ACM with SBGFLS model cannot handle intensity inhomogeneity in adjacent regions. Moreover, the gradient-based functions cannot converge zero at fuzzy object boundary.

Our proposed model includes the eigenanalysis of the Hessian matrix. Actually, the computation of Hessian matrix is a time consuming process. We give detailed explanations about computing the Hessian matrix in Section 4.5.

In proposed model, potential edge points are extracted by exhaustively searching for the extrema points (i.e. global minimum/maximum) in scale spaces. Accurate localization of boundary pixels is performed by Taylor expansion of input image. Hessian matrix and eigenvalues are used to eliminate the undesired edges with robust edge pixel responses at maximum curvature orientation. Thus the level set function has a larger capture range and capacity of anti-edge leakage. Hessian matrix encodes both shape and information of boundary pixel. Compared with the ACM with SBGFLS model, our

model uses local principal curvature information of boundary pixels (i.e. eigenvalues), the ACM with SBGFLS model uses the statistical information of boundary regions.

#### 4. Experimental results

In this section we present comprehensive results of our active contour model obtained in task of boundary detection. The evaluation metrics are used to show segmentation accuracy. Then we interpret the segmentation results of our model in detail using various test images. In addition, we compare the proposed model with recently developed ACMs by the same evaluation metrics. Finally, we compare our model with other state-of-the-art ACMs in terms of the computational efficiency and iteration number. All the experiments have been implemented in Matlab 2014 programming environment on a 3.3 GHz Intel i5 personal computer.

##### 4.1. Evaluation metrics

Image segmentation methods use a criterion to compare the accuracy of the segmentation results. The general evaluation metrics are the Probabilistic Rand Index (PRI) [46] and the Object-level Consistency Error (OCE) [47]. These functions evaluate the amount of overlap between ground-truth segments and segments obtained by the segmentation method [48,49]. However, there are some boundary based evaluation methods, like Pratt's Figure of Merit (FOM) [50] and Receiver-Operator-Characteristics (ROC) [51]. The FOM is calculated as,

$$FOM = \frac{1}{\max\{E_D, E_I\}} \sum_{i=1}^{E_D} \frac{1}{1 + \alpha \times (d_i)^2} \quad (19)$$

where  $E_I$  denotes the number of ground-truth edge pixels,  $E_D$  denotes the number of edges pixels extracted by the proposed model [47,52].  $d_i$  shows the distance from the  $i$ th detected boundary pixel to nearest ground-truth boundary pixel. The scaling constant  $\alpha$  is set to  $\alpha = 1/9$  for a penalization constant of misplaced edge points. If the FOM value is 1, segmentation model has maximum similarity ratio between the ideal and detected boundary pixels [50,53].

We also calculate the mean square error (MSE) to compare the segmentation results [54]. The MSE function evaluates the similarity measurement between the segmentation results and the ground truth. This metric is defined as,

$$MSE = \frac{1}{MN} \sum_{i=1}^M \sum_{j=1}^N (g(i, j) - s(i, j))^2 \quad (20)$$

where  $g(i, j)$  and  $s(i, j)$  are the ground-truth image and segmented image, respectively.  $i$  and  $j$  state the pixel position of the image. The smaller MSE values denote the less difference between the ground truth and the obtained segmentation results [55]. Thus, a smaller MSE corresponds to a better segmentation result.

On the other hand, Probabilistic Rand Index is also used to measure the similarity of the segmented region obtained using our model and multiple ground-truth images [46,56]. Consider a set of manual segmentations  $\{S_1, S_2, \dots, S_K\}$  of an image  $X = \{x_1, \dots, x_N\}$  consisting of  $N$  pixels. Let  $S_{test}$  be the segmentation that is to be compared with the ground-truth images. We denote the label of point  $x_i$  by  $l_i^{S_{test}}$  in segmentation  $S_{test}$  and by  $l_i^{S_k}$  in the ground-truth image. Then, the Probabilistic Rand Index is defined as

$$PRI(S_{test}, \{S_k\}) = \frac{1}{\binom{N}{2}} \sum_{\substack{i,j \\ i < j}} \left[ p_{ij}^{c_{ij}} (1 - p_{ij})^{1-c_{ij}} \right] \quad (21)$$

where  $p_{ij}$  denotes the expected value and  $c_{ij}$  denotes the event of a pair of pixels  $i$  and  $j$  having the same label in the test image  $S_{test}$ :

$$c_{ij} = \mathbb{I}(l_i^{S_{test}} = l_j^{S_{test}}) \quad (22)$$

The PRI takes values in  $[0, 1]$ , where means  $S_{test}$  and  $\{S_1, S_2, \dots, S_K\}$  have no similarities and 1 means all segmentations are identical [46].

##### 4.2. Experiments and discussions

In the experiments, our active contour model is tested and compared with the C-V model [8], the ACM with SBGFLS model [19], the ORACM model [20], the RSF model [6], the LIF model [26] and the LSACM model [7] in terms of segmentation accuracy and computational cost (iteration count and elapsed CPU time). These are well-known level set methods to image segmentation.

For the C-V model, the parameter of smoothing term and the parameters of the constant terms were set to  $\mu = 1$  and  $\lambda_1 = \lambda_2 = 1$ . The ACM with SBGFLS contains a constant parameter  $\alpha$  given at Eq. (8). To make a fair comparison,  $\alpha$  is

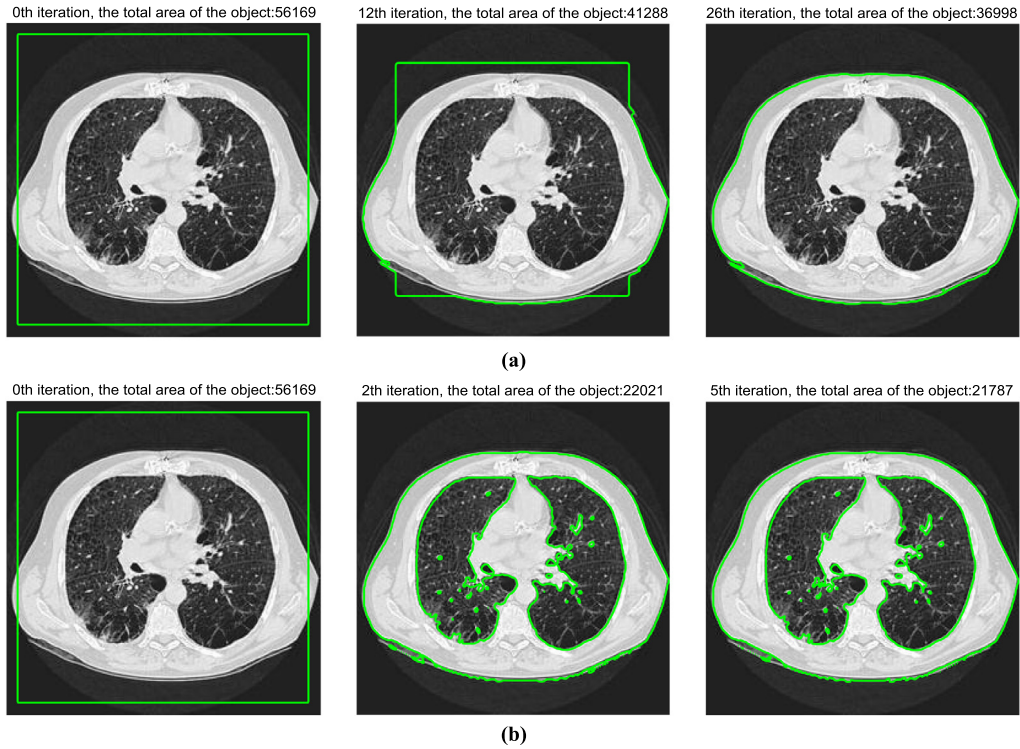


**Fig. 5.** Global segmentation results of medical image. (a) ACM with SBGFRLS ( $\alpha = 25$ ) (b) The proposed model.

**Table 1**

Comparison of FOM and PRI results for ACM with SBGFRLS and our proposed models. The bolded values represent the best FOM values.

	ACM with SBGFRLS		Our proposed	
	FOM	PRI	FOM	PRI
Fig. 5	0.1426	0.236	<b>0.6945</b>	<b>0.704</b>
Fig. 6	0.7694	0.827	<b>0.8952</b>	<b>0.902</b>

set to 25 and 10. The RSF model uses many constant parameters. We use the following parameters in experiments:  $\sigma = 3$ ,  $\lambda_1 = \lambda_2 = 1$ ,  $\Delta t = 0.1$ ,  $\mu = 1$  and  $\nu = 10.001 \times 255 \times 255$ . It should be noted that in the experimental analysis of the RSF model, the larger  $\sigma$  values can produce more stable results. Therefore, we used different  $\sigma$  values for some images. The parameters of LIF model are set as:  $\rho = 1$ ,  $\varepsilon = 1.5$ ,  $\varsigma = 0.5$  and  $\Delta t = 0.025$ . Parameter  $\sigma$  is selected by experience according to the input images. The LSACM model has three basic parameters:  $\Delta t$ ,  $\varepsilon$  and  $\rho$ . The time step for level set evolution is set  $\Delta t_1 = 0.1$ , and then it is set  $\Delta t = 0.1$ . In most experiments, we set  $\varepsilon = 1$  and  $\rho = 6$ . For RSF, LIF and LSACM models, it should be noted that small  $\rho$  reduces computational burden in each iteration. The total number of iterations required to convergence is given in the related tables for each experiments. Our model uses only  $\sigma$  parameter. In this paper, we fixed parameter  $\sigma = 1$  for all test images. Experiments have been carried out for consumer and medical images, and the obtained algorithm results are evaluated together for a more accurate comparison. Finally, all experiments have been carried out with similar initial contours (with respect to positions) for the input images.

In the first experiment (Fig. 5), a human lung CT image is used to confirm the effectiveness of the proposed active contour model. The evolution stages of the active counter are shown. We compared performance of our method with that of the ACM with SBGFRLS in terms of iteration number and total object area. The anterior and posterior boundary regions between the left and right lungs are quite thin. The goal of the lung segmentation process is to detect these boundary lines and extract the right and left lung regions. Fig. 5a (first image) shows initial curves. The ACM with SBGFRLS can detect only exterior boundaries of lung CT image after 26 iterations. Fig. 5b shows the abilities of the proposed active contour model for lung boundary separation. The proposed method can extract both interior and exterior boundaries of the image after only 5 iterations. Moreover, our model efficiently obtains mediastinum, pulmonary arteries and vein region boundaries. In Table 1, the FOM and PRI values are given to show the quality of the segmentation results by the two models.

A real image is used in the second experiment. The ground-truth segmentation image is obtained manually. The improvement of our model can be seen step by step in Fig. 6. As shown in the first row of Fig. 6a and Fig. 6b, the initial

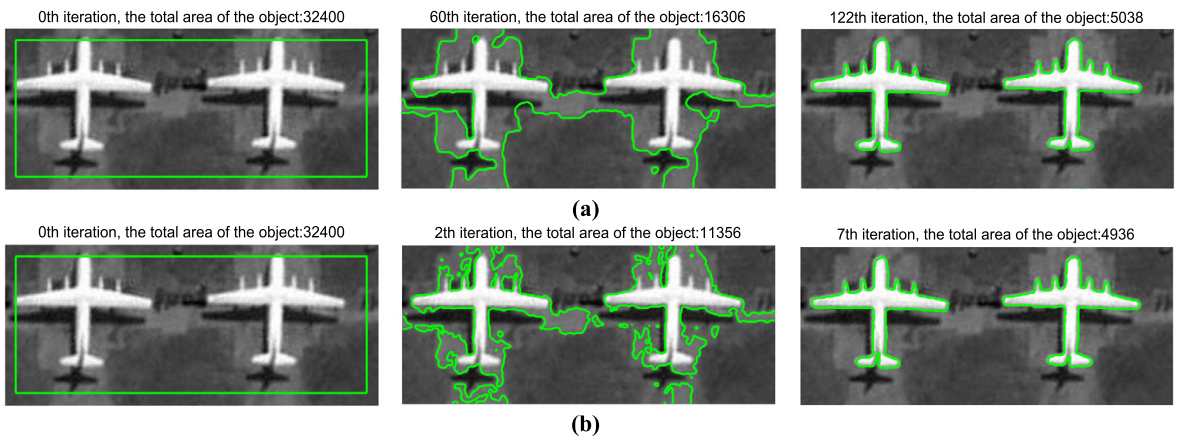


**Fig. 6.** Global segmentation results of consumer image. (a) ACM with SBGFLRS ( $\alpha = 10$ ) (b) The proposed model.

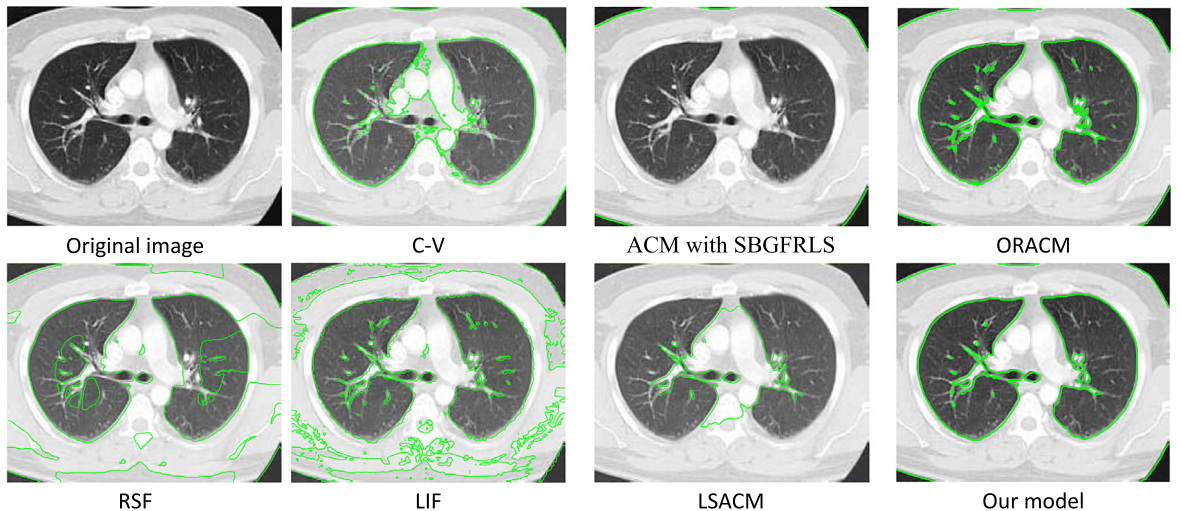


**Fig. 7.** Segmentation results of real lung CT image.

active contour is far from the object boundaries. Fig. 6b presents segmentation results of our model. The proposed model could efficiently detect all the object boundaries. The proposed level set function converges in only 7 iterations and takes only 0.31 s while the ACM with SBGFLRS model converges in 122 iterations and takes for 51 s. Similar to the first experiment, superiority of the proposed model on real images can be seen in the second experiment. In Table 1, the FOM value is computed to express the accuracy of the segmentation results of a real image. According to the FOM and PRI values, our proposed model achieves better segmentation results than the ACM with SBGFLRS model.

For a better comparison and numerical analysis, we compared the seven models on seven medical images and observed the segmentation results. Firstly, Fig. 7 shows the segmentation results on a real lung CT image. The ground-truth segmentation image is obtained manually. The C-V method can extract the interior region contours of lungs, while the ACM with SBGFLRS cannot extract the contours in interior area of image. Hence, the ACM with SBGFLRS produces a very large gap between left and right lungs. The ORACM and the proposed method can segment both interior and exterior region boundaries of the lung CT image successfully. The proposed model enters into the interior region efficiently and detects the object boundaries. Since the strength of intensity inhomogeneity is strong, the performances of RSF and LIF models also reduce. Thus, these models perform over-segmentation. The contour of the LSACM model cannot detect important parts of the lung boundary. Compared with our model, the LSACM cannot work well on mediastinum, pulmonary arteries and vein region regions. We notice that the segmentation performances of RSF, LIF and LSACM models are considerably sensitive to the choice of scale parameter  $\sigma$ . A too small scale parameter may produce undesirable segmentation result. Thus,  $\sigma$  parameter should be selected according to the input image.

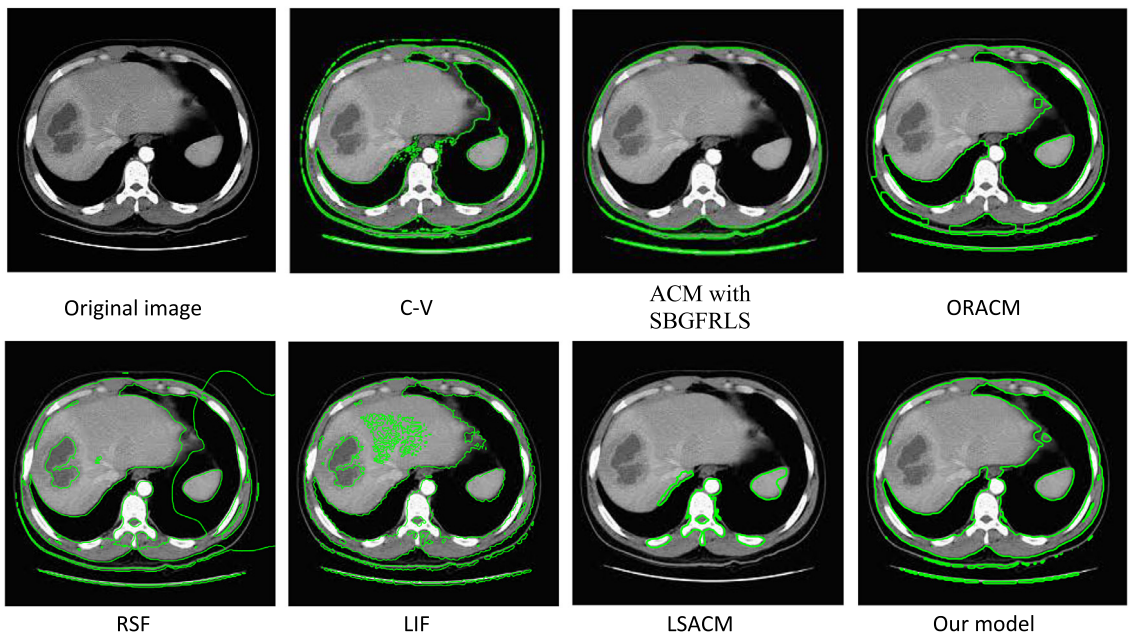


**Fig. 8.** Segmentation results of real liver CT image.

**Fig. 8** shows the segmentation results for liver segmentation. The curve is initialized by a large closed rectangle outside the liver. The ACM with SBGFRRLS and LSACM models cannot obtain the interior contour of liver. Although the seven initializations are completely same, the proposed model extracts correct boundaries of the liver regions. Furthermore, the ORACM and our method correctly separate the Spleen, Liver and Aorta regions of liver CT image. It should be noticed that the segmentation accuracy of our model is a little bigger than the ORACM model in terms of the measures of FOM and MSE since our model effectively detects the liver parenchyma and vessels regions. The RSF model detects some liver lesion areas, but it performs over-segmentation.

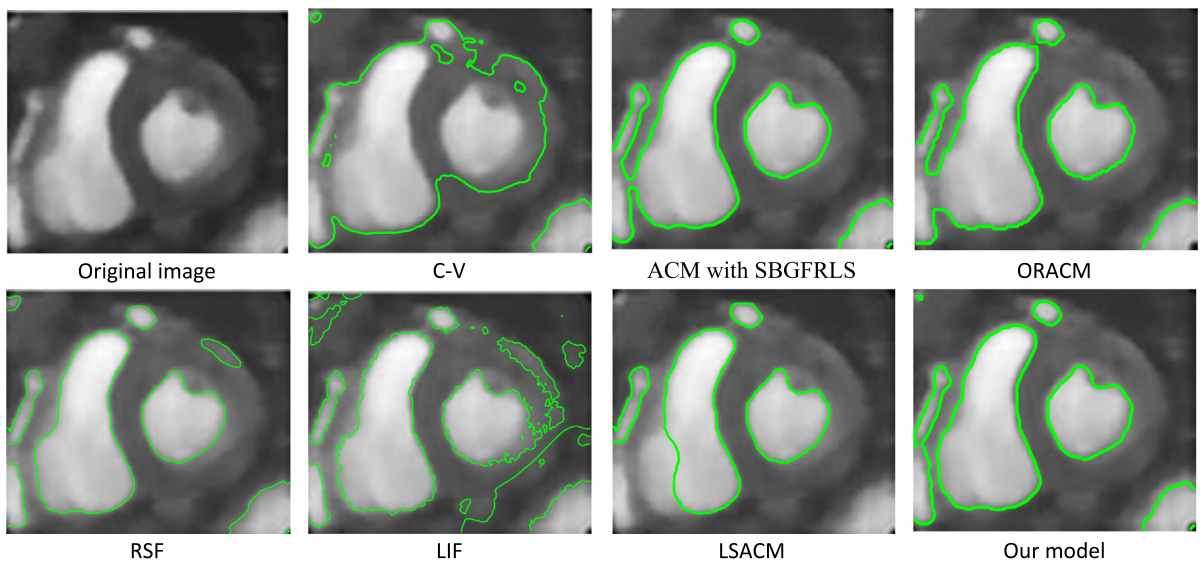
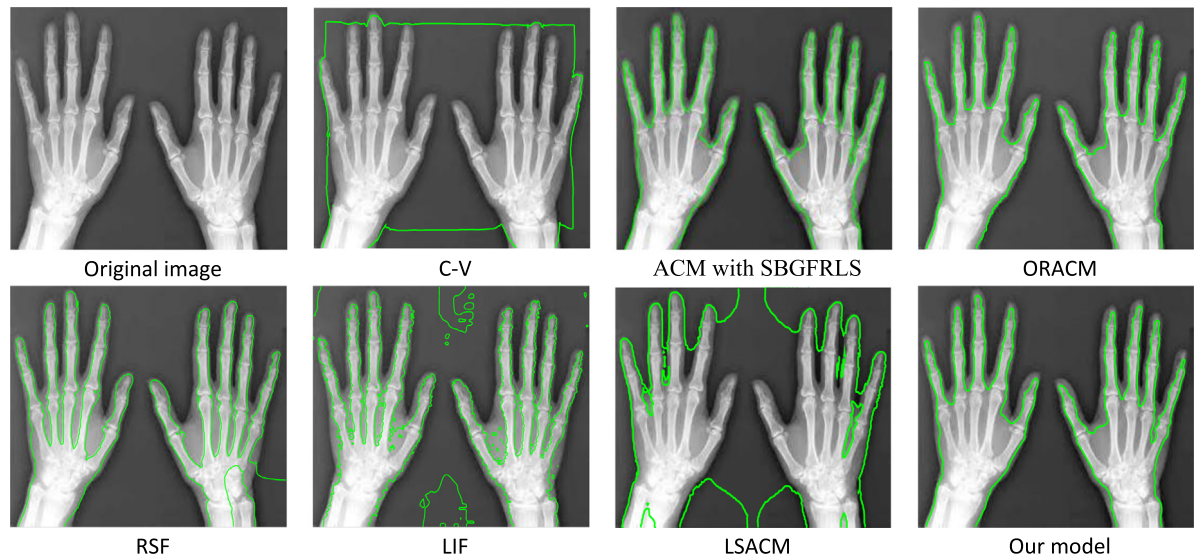
We also tested the proposed model on the cardiac MR image segmentation. **Fig. 9** shows the ventricle segmentation results on cardiac MR image. The automated segmentation of left and right ventricles is a difficult task. This difficulty results from the complex anatomy of the heart and low contrast. The ACM with SBGFRRLS, ORACM, RSF and LSACM models obtains more accurate results than the C-V and LIF models. As it is shown in **Fig. 9**, our model accurately obtains boundaries for the left and right ventricles. It shows that all the models perform relatively well on the right ventricle. However, on the left ventricle, CV, LIF and LSACM models obtain broken contours. The C-V model misses a large part of the left and right ventricles.

For X-ray hand image, accurate results similar to cardiac segmentation are obtained. The initial curve is initialized by a large closed rectangle outside the image. Except for ACM with SBGFRRLS, ORACM and our model, all other active contour models have failed. The RSF model has tracked the bones on hand rather than segmenting the boundary. In **Fig. 10** also we can see that RSF and LIF models have tracked the bones of fingers well but rest of the bones are not segmented. The C-V, LIF and LSACM models have completely failed by tracking boundary of hand. However, use of intensity information in image regions at a specific scale in both RSF and LIF models can provide acceptable segmentation results for some images.

**Fig. 11** shows the segmentation results of brain CT image. Parameter  $\sigma$  of RSF, LIF and LSACM models is chosen as 6, 10 and 10, respectively. The contour initializations of seven models are very similar, but the final contour evaluations are very different, which confirm the robustness of our model to similar initializations. The CV model can only detect scalp and skull brain regions successively. The ACM with SBGFRRLS model gives similar failure segmentation result. In addition to these regions, the proposed method can also detect lateral ventricles in interior side of brain. The ORACM and LIF models generally fail in segmentation of significant brain regions. Several brain regions are wrongly segmented. Since the ORACM model uses block thresholding process, it produces rigid object boundaries.

In **Table 2**, the FOM and PRI results are presented to show the accuracy of the segmentations results by the seven models. The proposed model has the best FOM and PRI values while the ORACM model operates slightly better than the ACM with SBGFRRLS, RSF and LIF models. Moreover, the MSE results are shown in **Fig. 12**. Except lung CT image, we can see that the proposed model has the smallest MSE results among the seven models.

To show the performance of the models, we also used three retinal images from the Stare database [57]. The Stare database consists of 400 retinal images and their ground truth images. The retinal images in Stare database were captured using a fundus camera, and digitized at  $305 \times 700$  pixels in resolution [57]. To visualize the segmentation results more clearly, original retinal images are firstly zoomed. Then, zoomed block sub-images are produced by using cropping process, and

**Fig. 9.** Segmentation results of real cardiac MR image.**Fig. 10.** Segmentation results of real X-ray hand image.**Table 2**

Comparison of FOM and PRI results obtained by different models. The bolded values represent the best FOM values.

	C-V		ACM with SBGFLRS		ORACM		RSF		LIF		LSACM		Our model	
	FOM	PRI	FOM	PRI	FOM	PRI	FOM	PRI	FOM	PRI	FOM	PRI	FOM	PRI
Fig. 7	0.475	0.483	0.154	0.164	<b>0.630</b>	<b>0.687</b>	0.384	0.395	0.320	0.348	0.176	0.194	0.624	0.646
Fig. 8	0.484	0.502	0.214	0.226	0.538	0.557	0.394	0.397	0.425	0.442	0.134	0.168	<b>0.542</b>	<b>0.681</b>
Fig. 9	0.280	0.341	0.584	0.594	0.598	0.605	0.600	0.628	0.304	0.327	0.516	0.603	<b>0.604</b>	<b>0.638</b>
Fig. 10	0.107	0.241	0.573	0.603	0.699	0.715	0.526	0.564	0.376	0.391	0.210	0.346	<b>0.701</b>	<b>0.743</b>
Fig. 11	0.478	0.581	0.584	0.612	0.407	0.538	0.632	0.639	0.501	0.547	0.548	0.559	<b>0.746</b>	<b>0.791</b>

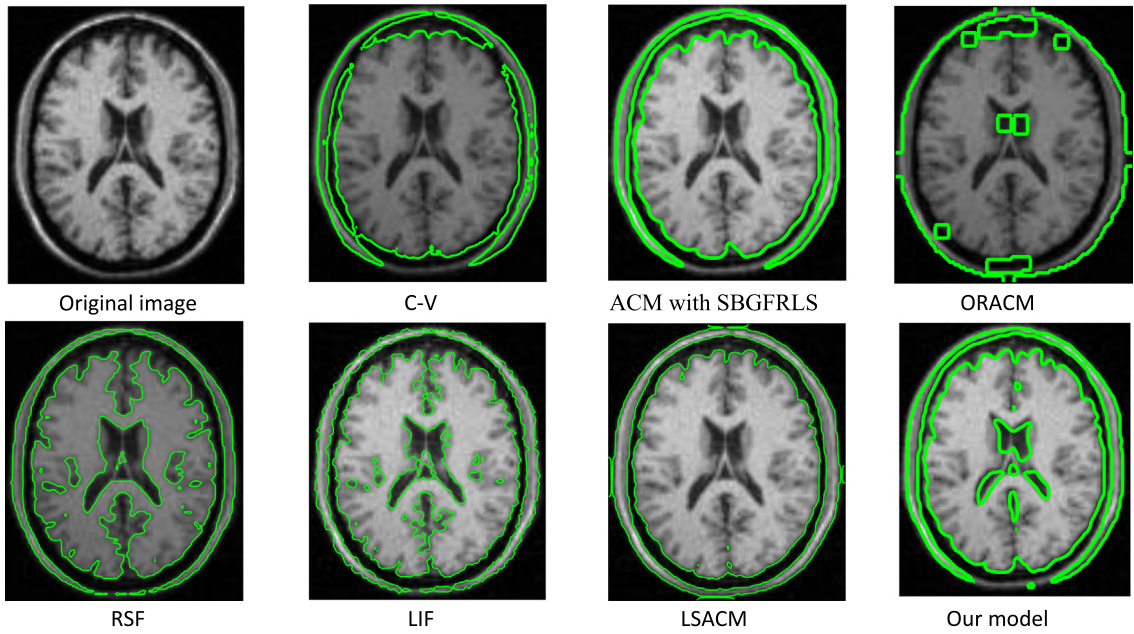


**Fig. 11.** Segmentation results of real brain CT image.

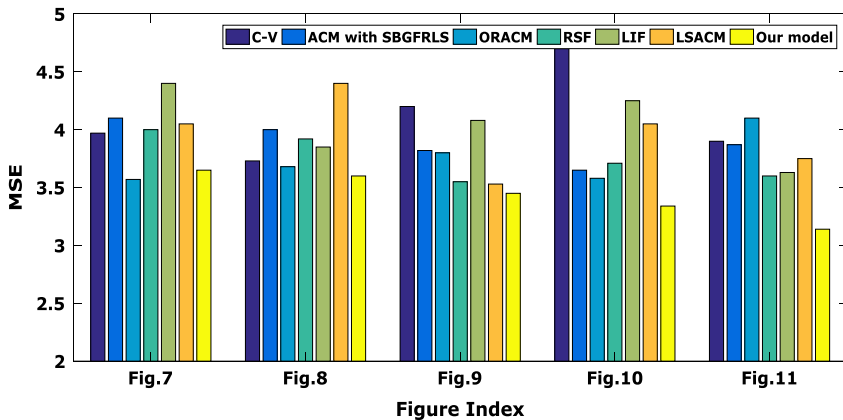


**Fig. 12.** The values of MSE for the medical images in Figs. 7–10 and 11. Generally, the MSE errors of our model are smaller than that of the other seven models.

they are used in experiments. All segmentation results are given in Figs. 13, 14 and 15. The C-V and LIF models fail in vessel extraction process. In general, the ACM with SBGFRLS, ORACM and LSACM models lose some tiny vessel structures. Since the widths of retinal vessels vary from very large (15 pixels) to very small (3 pixels), automated and online retinal image segmentation is a challenging task. Thus, the ORACM model cannot detect thin vessels that are depicted in Fig. 13. The proposed model is able to detect vessels with varying thicknesses. The intensity on the vessel line is lowest. Naturally, the LIF model cannot detect vessel lines.

For the retinal images in Figs. 14 and 15, the ACM with SBGFRLS, ORACM and LSACM models almost gives similar result with the result of our model. The vessel images have intensity inhomogeneities. For the images with intensity inhomogeneities, the C-V model cannot be applied well. On the other hand, the LIF and LSACM models are more efficient than the C-V model. Since the image intensity inside or outside the active contour curve is inhomogeneous, the C-V and LIF models cannot detect right vessel boundaries.

The LSACM model is different from the RSF model due to the following reasons. Compared to the LIF model, the LSACM model has different characteristics. In the LSACM model, the variances of the Gaussian distributions are piecewise constant in each region, and these properties making LSACM model more stable than the LIF model. The LSACM model also uses a

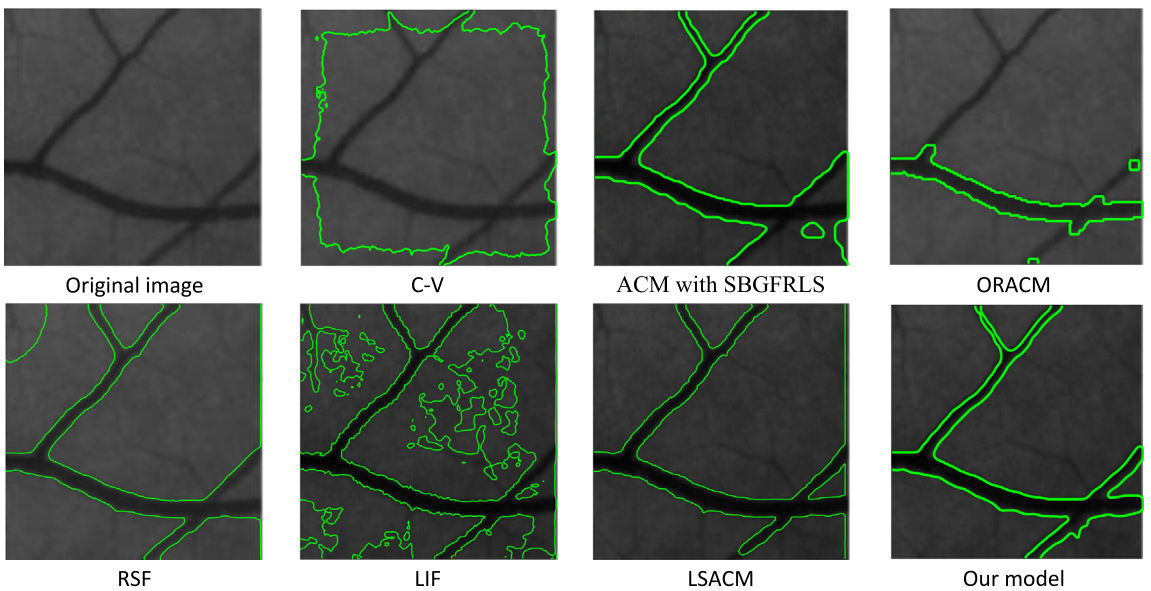


**Fig. 13.** Segmentation results of cropped and zoomed retinal image.

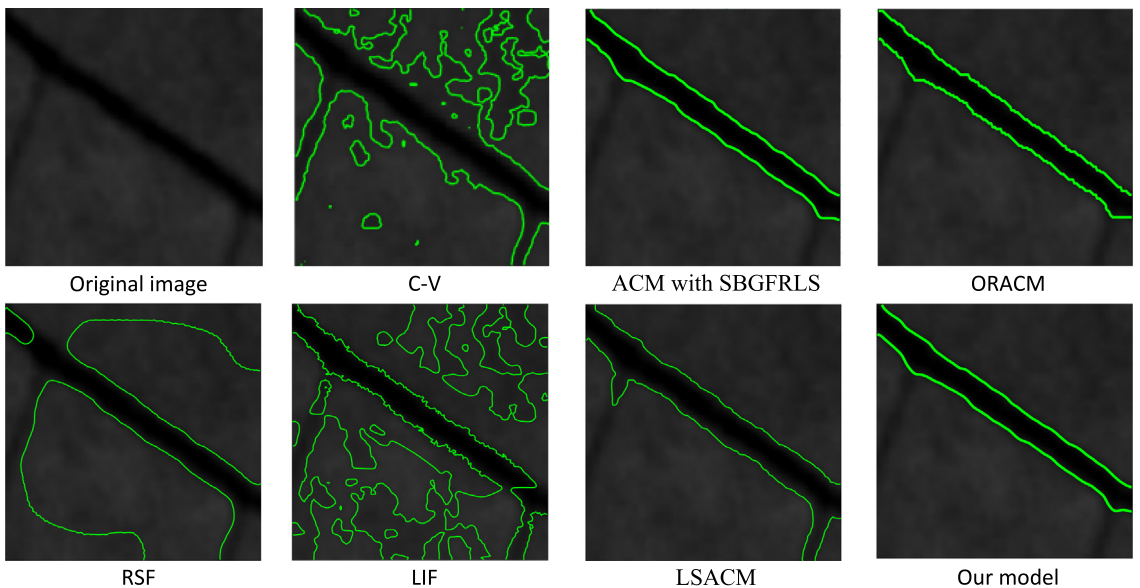


**Fig. 14.** Segmentation results of cropped and zoomed retinal image.

constant kernel to identify a local region; as a result, principal parts of the background/foreground are correctly identified. We can see that the proposed model can detect both thin and thick retinal vessels, as shown in [Fig. 15](#).

Moreover, combining the superiorities of the eigenvalues of the Hessian matrix and the *spf* function, the vessel regions are better segmented. Although the Hessian matrix has strong response in the vessels regions, it does not have large eigenvalues at the crossing vessel regions. Thus, second order derivative-based segmentation algorithms generally fail to detect the interior vessel boundaries when the initial active contour is far from the interior object boundary. It is worth pointing out that our level set formulation in Eq. (14) uses a *spf* function, and it deals with this situation. Since the *spf* function has opposite signs around the object boundary, active contour can shrink when it is inside the object when outside the object it expand. Hence, it can be inferred that the *spf* function and the eigenvalues of the Hessian matrix are complementary and their combination can effectively detect vessel regions in comparison with either of them alone.

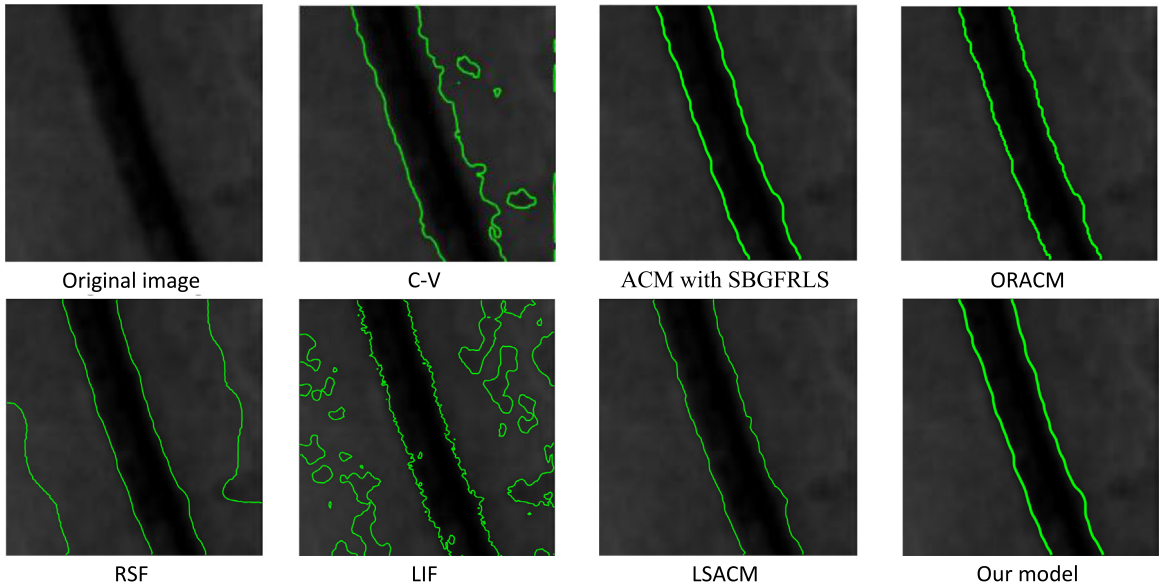


**Fig. 15.** Segmentation results of cropped and zoomed retinal image.

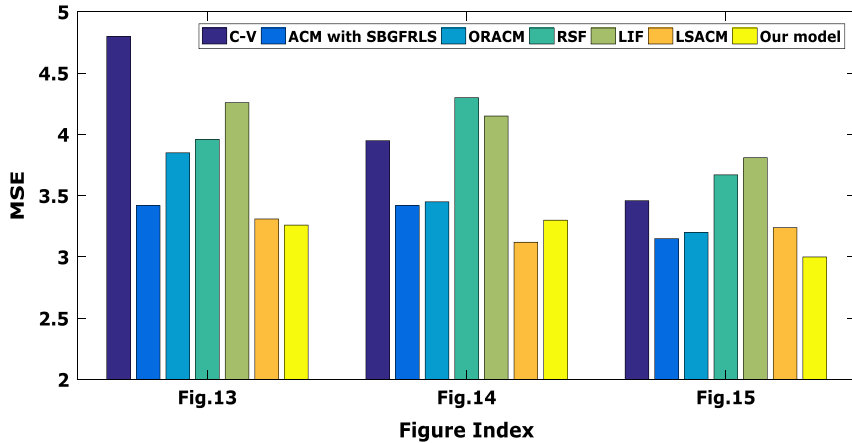


**Fig. 16.** The values of MSE for the retinal images in Figs. 13, 14 and 15. Generally, the MSE errors of our model are smaller than that of the other seven models.

On the other hand, Jin et al. [31] proposed a Hessian-based filtering combined with the C-V model. The highest segmentation result is 98.14%. They used Hessian matrix and eigenvalues to enhance medical images. Therefore, the level set function does not use Hessian matrix. Moreover, it needs the initial active contour obtained by the Otsu's thresholding method [58]. In our model, we use directly Hessian matrix and eigenvalues in the level set function. This is a considerable situation since the two models are based on absolutely different assumptions. The first method is based on an enhancement process of the medical image while our method is based on the Hessian-based level set function, which contains all the information of the eigenvalues.

In Table 3, the FOM and PRI results are given to show the accuracy of the segmentations results by the seven different ACMs. The FOM and PRI results show that our model has the best segmentations quality for all tested retinal images. Fig. 16 shows that the MSE values of our model are more efficient than the other ACMs. As shown in Fig. 16, the proposed model with the Hessian term and *spf* function detects the object boundaries better than the C-V, ACM with SBGFRLS, ORACM, RSF, LIF and LSACM models.

In the following discussion, we mention some advantages of our model in terms of smoothness. Although the ORACM and our model give similar segmentation results in terms of accuracy in the above experiments, the segmentation result of our model has a greater smoothness than the ORACM model. Since our model uses the Gaussian filter to enhance and

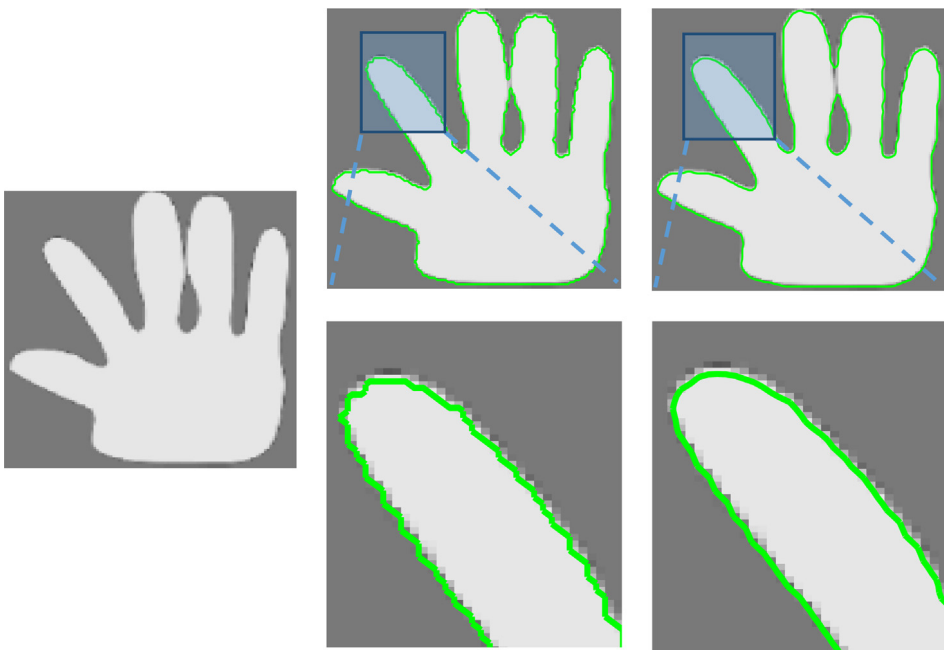


**Fig. 17.** Comparison between the ORACM and the proposed model on synthetic image. The first column shows the original image, second and third columns show segmentation results of the ORACM and the proposed model, respectively.

**Table 3**

Comparison of FOM and PRI results obtained by different models. The bolded values represent the best FOM values.

	C-V		ACM with SBGFLS		ORACM		RSF		LIF		LSACM		Our model	
	FOM	PRI	FOM	PRI	FOM	PRI	FOM	PRI	FOM	PRI	FOM	PRI	FOM	PRI
Fig. 13	0.104	0.197	0.658	0.684	0.301	0.376	0.591	0.644	0.214	0.226	0.662	0.724	<b>0.756</b>	<b>0.811</b>
Fig. 14	0.273	0.294	0.798	0.821	0.760	0.817	0.320	0.384	0.241	0.287	0.831	0.862	<b>0.804</b>	<b>0.874</b>
Fig. 15	0.641	0.694	0.887	0.913	0.874	0.916	0.602	0.644	0.394	0.435	0.842	0.891	<b>0.899</b>	<b>0.934</b>

**Table 4**

The specific properties of the active contour models.

Properties	C-V	ACM with SBGFLS	ORACM	RSF	LIF	LSACM	Our model
Online	×	×	✓	×	×	×	✓
Smooth boundary	✓	×	×	✓	✓	✓	✓
Use level sets	✓	✓	✓	✓	✓	✓	✓
Color images	✓	×	×	×	×	×	✗

smooth object boundaries. Gaussian filter is a low pass filter, and thus applies smoothing and regularization to the level set function. On the other hand, ORACM model uses the morphological enhancement based on opening and closing operations to correct the segmentation results. Usually, the enhancement results of ORACM model in boundary regions are not satisfactory because object boundaries may have multiple orientations. The segmentation results of two models on a synthetic hand image are shown in Fig. 17. The first column demonstrates the original image, and the second and third columns show the results of the ORACM and the proposed model, respectively. The results at second row are obtained by zooming original segmentation results shown at first row.

Table 4 presents the differences between the proposed model and the traditional ACMs. For better understanding of the differences between algorithms, the key properties are represented in Table 4 in brief. As it is shown, the ORACM method cannot produce smooth object boundary, but, the proposed model can extract right and smooth object boundaries. In addition, although the ORACM can run online, it is not as fast as the proposed model. However, the proposed model cannot be used for color images. Since the RSF, LIF and LSACM models have high computational time, they cannot be used in online segmentation applications.

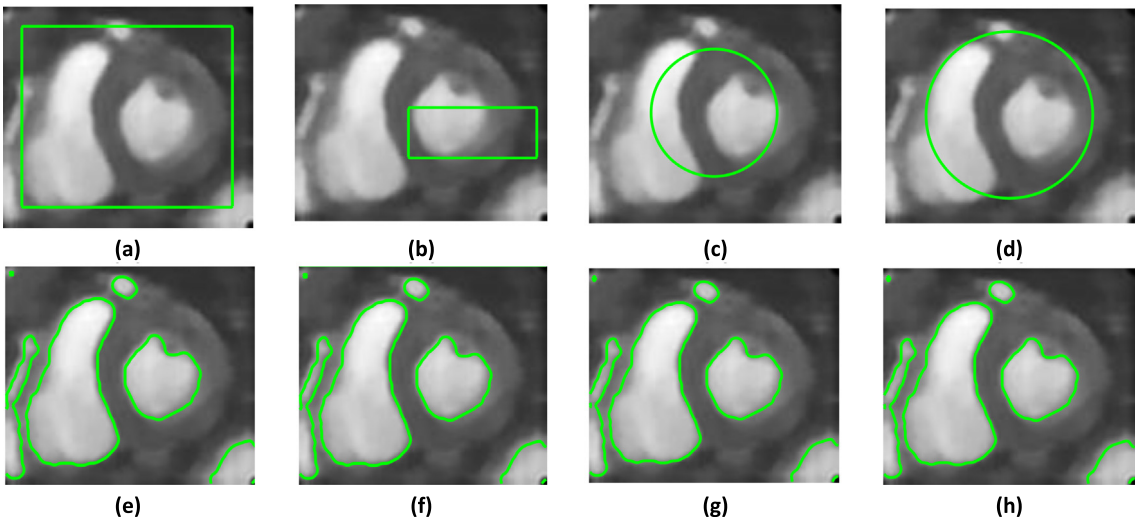


**Fig. 18.** Cardiac MRI image with (a)–(d) different initial contour positions; (e)–(h) are corresponding extracted contours.

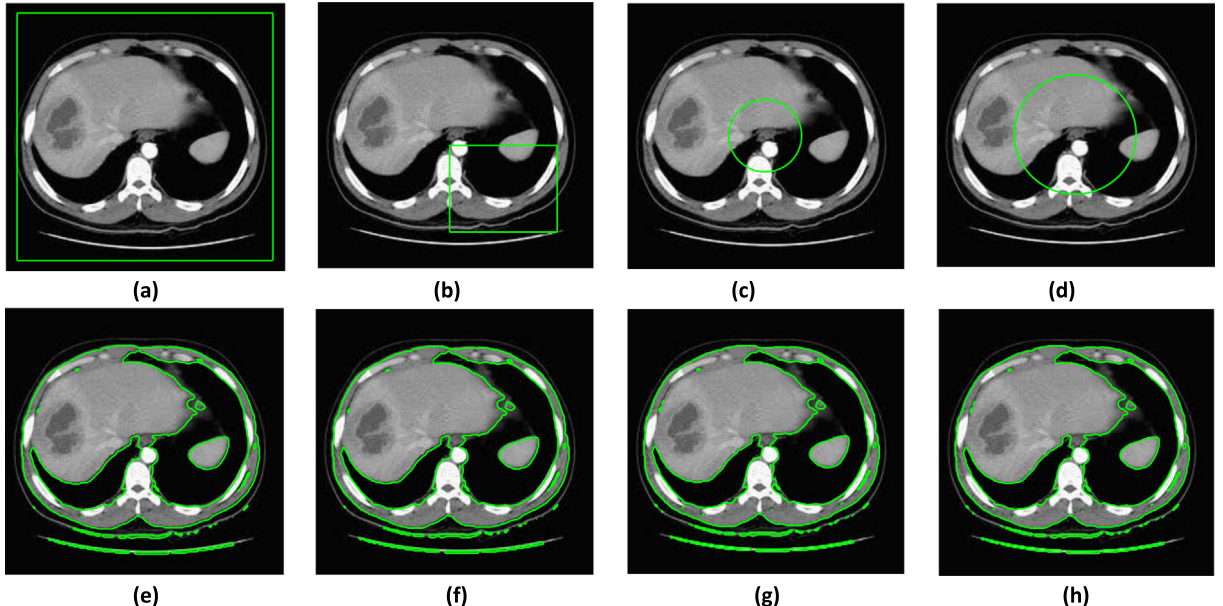


**Fig. 19.** Lung CT image with (a)–(d) different initial contour positions; (e)–(h) are corresponding extracted contours.

#### 4.3. Effect of initial contour position

In our model, the active contour is iteratively evolved with an initialization. When the energy function presented in Eq. (15) is minimum, the optimal active contour is calculated. If the energy function of model is convex, it is easy to obtain global contour with an iterative procedure. Our energy function (given in Eq. (15) as a minimization problem) can be solved by the gradient descent method. Also, the proposed energy function is convex in nature. Thus, minimization of the proposed energy function is independent of the initial contour position. In this section, this statement is verified experimentally. Cardiac MRI, lung CT and brain CT images with different initial contours (see Figs. 18(a)–(d), 19(a)–(d) and 20(a)–(d)) are considered. Figs. 18(e)–(h), 19(e)–(h) and 20(e)–(h) show the extracted contours corresponding to each initialization. From these results, it is seen that for different initializations, the proposed model produces satisfactory segmentation results. From the experimental results, it is also concluded that the quality of segmentation results using the proposed model is independent of the initial contour position.

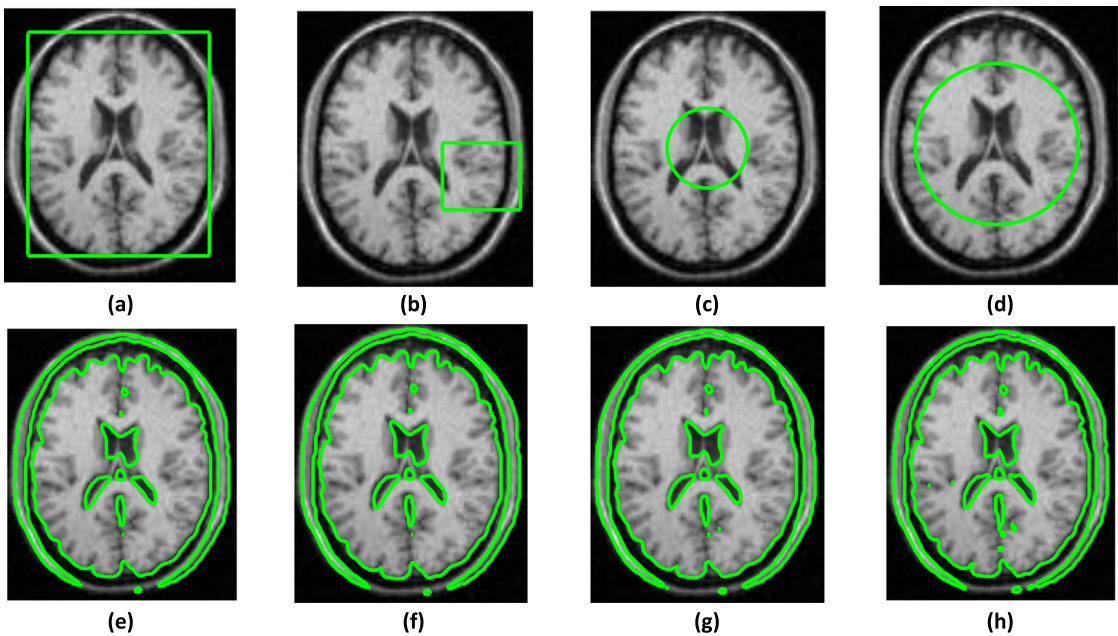


**Fig. 20.** Brain CT image with (a)–(d) different initial contour positions; (e)–(h) are corresponding extracted contours.

#### 4.4. Effect of noise

The last experiment tests the effect of noise on the segmentation results. Fig. 21 and Fig. 22 show the segmentation results of synthetic and medical images with objects having interior holes. The images were added with Gaussian noise with standard deviation 0.05. To assess the superiority of the proposed model, their results were compared with the C-V, ACM with SBGFLS, ORACM, RSF, LIF and LSACM models in terms of segmentation result, CPU time and iteration count. The results of the C-V model are shown in Figs. 21 and 22, which are not good. Besides, for the synthetic image, our model obtains good segmentation results in only 4 iterations, while the Chan–Vese model still does not get final segmentation results even after 30 iterations. Moreover, the C-V model performs over-segmentation in the trachea regions. From Fig. 21, we can observe that the right segmentation result cannot be obtained from the ACM with SBGFLS model. The main drawback is that parameters of ACM with SBGFLS model heavily affect the segmentation results, especially when we select a small standard deviation  $\sigma$ . If a small  $\sigma$  is selected, the regularized ability of Gaussian filter will be weak. In noise experiments, we use different  $\sigma$  values, which range from 0.7 to 1.5. On the other hand, the ACM with SBGFLS model also uses a constant  $\alpha$  parameter. The value of  $\alpha$  is set according to input images. To obtain best segmentation results in noisy images,  $\sigma$  and  $\alpha$  parameters are set to 1 and 25, respectively. For the synthetic image, the ACM with SBGFLS model can flow into narrow regions, but it cannot segment the lung CT image with low contrast and noise. The LIF model uses the local pixel intensity to fit the noisy intensities of the images. Thus, it obtains better segmentation results than the RSF and LSACM models on images with intensity inhomogeneity. Since the addition of Gaussian noise increases the boundary region inhomogeneity, LIF, RSF and LSACM models are unable to segment lung CT image in noisy environment. In addition, Gaussian noise reduces the high contrast in the image, and this situation causes unsatisfactory segmentation result. ORACM model successfully extracts the object boundaries of synthetic image, while it cannot segment the lung CT image. However, use of gradient and morphological operations based local information in both ACM with SBGFLS and ORACM models provides acceptable segmentation results for synthetic noisy images. It can be seen that the pixel intensities within right and left lungs become quite inhomogeneous. Due to the presence of noise components in the considered medical image, the boundaries of right and left lungs are not extracted by the ACM with SBGFLS and ORACM models. On the contrary, the proposed model using eigenvalues of the Hessian matrix extracts the best segmentation results of different lung regions for image corrupted by Gaussian noise. It is worth pointing out that, although the segmentation accuracy of our model is not so perfect, it is explicitly better than the other models. The total iterations, the elapsed time (in seconds) and the corresponding FOM values are presented in Table 5.

Table 6 shows the FOM metrics obtained by different models. It indicates that the proposed model is more efficient than all other models for segmenting noisy images.

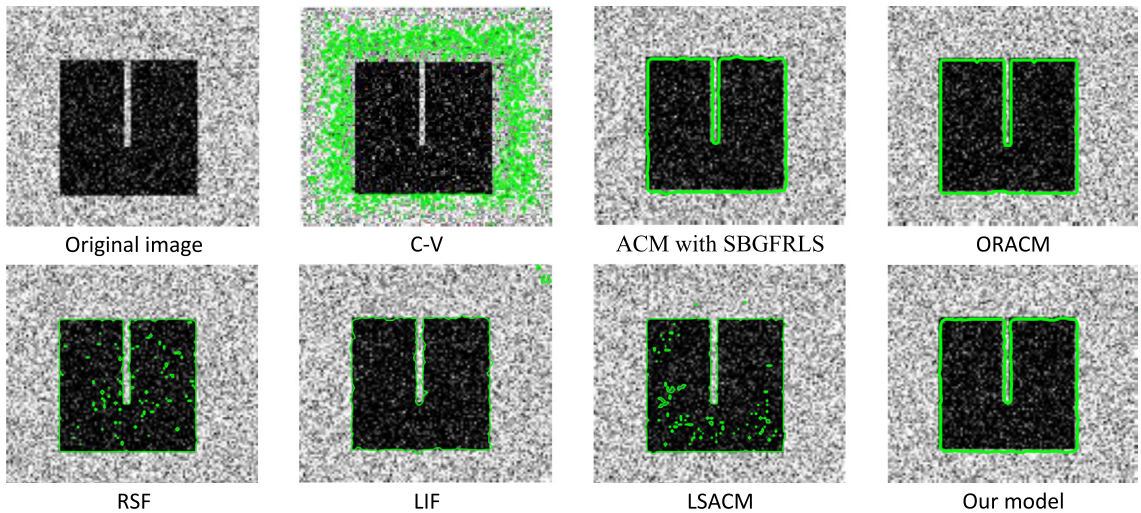


**Fig. 21.** Segmentation results on synthetic image containing Gaussian noise.

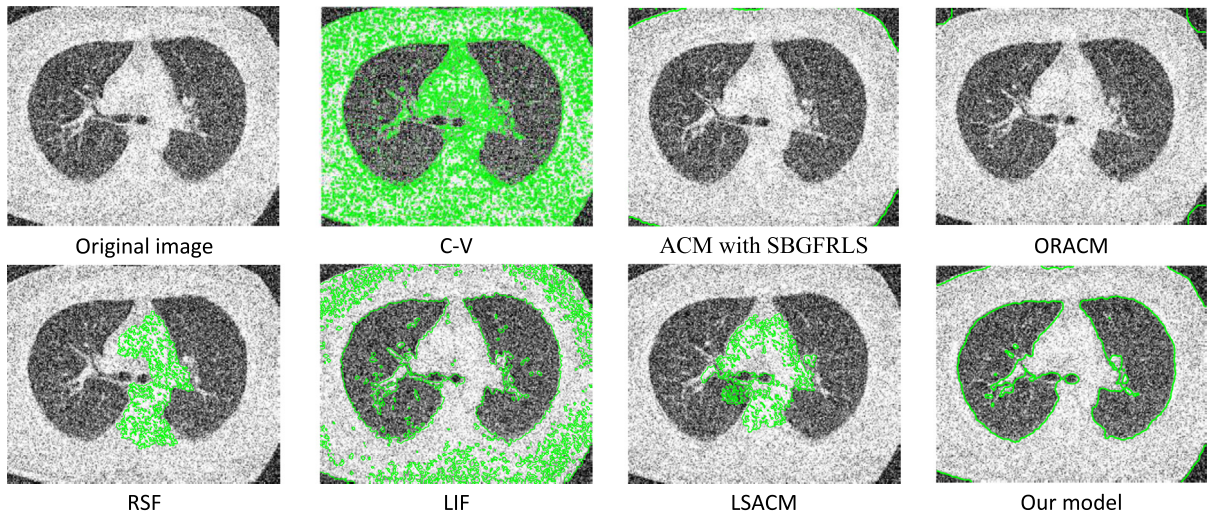


**Fig. 22.** Segmentation results on medical image containing Gaussian noise.

**Table 5**

The comparison results for the elapsed time (s) and the number of iterations. The bolded values represent the best calculation time and iteration number.

		C-V	ACM with SBGFLRS	ORACM	RSF	LIF	LSACM	Our model
<a href="#">Fig. 21</a>	Time	1.86	1.71	0.34	7.31	31.33	10.08	<b>0.16</b>
	Iteration	30	36	<b>3</b>	200	300	300	4
<a href="#">Fig. 22</a>	Time	123.54	0.66	0.73	3.30	15.24	4.40	<b>0.39</b>
	Iteration	257	9	8	200	300	300	5

**Table 6**

Comparison of FOM results obtained by different models. The bolded values represent the best FOM values.

	C-V		ACM with SBGFLRS		ORACM		RSF		LIF		LSACM		Our model	
	FOM	PRI	FOM	PRI	FOM	PRI	FOM	PRI	FOM	PRI	FOM	PRI	FOM	PRI
<a href="#">Fig. 21</a>	0.016	0.141	0.893	0.941	0.904	0.946	0.467	0.514	0.583	0.634	0.405	0.497	<b>0.908</b>	<b>0.942</b>
<a href="#">Fig. 22</a>	0.024	0.184	0.142	0.186	0.184	0.247	0.004	0.121	0.284	0.346	0.007	0.129	<b>0.627</b>	<b>0.713</b>

**Table 7**

The comparison results for the elapsed time (s) and the number of iterations. The bolded values represent the best calculation time and iteration number.

		C-V	ACM with SBGFLRS	ORACM	RSF	LIF	LSACM	Our model
<b>Fig. 7</b>	Time	236.08	0.6935	0.63	7.38	18.63	10.11	<b>0.32</b>
	Iteration	224	7	<b>4</b>	200	300	300	<b>4</b>
<b>Fig. 8</b>	Time	2532.50	46.02	2.78	5.87	17.97	10.79	<b>1.59</b>
	Iteration	392	86	<b>5</b>	200	300	300	<b>5</b>
<b>Fig. 9</b>	Time	26.62	12.04	0.69	4.62	3.65	4.57	<b>0.28</b>
	Iteration	114	55	<b>6</b>	200	300	300	<b>6</b>
<b>Fig. 10</b>	Time	4.22	37.93	1.06	451	42.36	11.36	<b>0.56</b>
	Iteration	23	67	6	200	300	300	<b>6</b>
<b>Fig. 11</b>	Time	2.13	1.17	0.58	4.38	6.91	4.21	<b>0.18</b>
	Iteration	19	14	5	200	300	300	<b>3</b>

#### 4.5. Computational complexity

Computational complexity of the proposed method is compared with state-of-the-art segmentation algorithms, such as ACM with SBGFLRS [19], fuzzy energy based active contour model [59], LIF [26] and inhomogeneity-embedded active contour (InH\_ACN) [60]. Before mentioning the computational complexity of the proposed method, it is necessary to explain complexity of the convolution operation. If the matrix padding operation is negligible, one 2D convolution operation (image with size  $(M, N)$  and filter mask with size  $(m, n)$ ) would have an approximate complexity of  $O(MNmn)$ . The values of  $(M, N)$  are larger than  $(m, n)$ . For example  $M = N = 800$  and  $m = n = 5$ .

The proposed method has one main function named as Main and two sub functions named as Hessian2D and Eig2image. Its computational complexity is given in detail in the [Appendix](#). The computational complexity of the main function is a simple linear combination of Hessian2D function, Eig2image function and while-loop block. The Hessian2D function consists of three convolution operations. Because of that, its computational complexity is  $O(3MNmn)$ . Eig2image function does not consist of convolution. It calculates the Eigenvalues from the Hessian matrices, sorted by abs value. Its computational complexity is  $O(21MN)$ . While-loop block in the Main Function has one convolution process and can be continued up to 50 times. The running cost of one loop is  $15MN + MNmn$ . Because of that, the while-loop cost is  $50(15MN + MNmn)$ . The total complexity of the Main Function is approximately  $O(53MNmn + 771MN)$ . If the variables are selected equal as  $M = N = (mn)^2$ , it can be represented as  $O(N^3)$  (see the [Appendix](#)).

Note that the proposed method does not use the functions of Hessian2D and Eig2image inside while-loop. This provides the superiority of the proposed method is faster than the gradient based ACMs.

ACM with SBGFLRS model has also similar while-loop operation. However, every loop in that method has three convolution operations. Two of them come from gradient calculation (horizontal and vertical) and the other is mask image and filter mask ( $\text{conv2}(u, G)$ ). This situation generates that the complexity is  $O(itr * 3 * MNmn)$ . The parameter  $itr$  shows the number of iterations.

For the fuzzy energy based active contour model [59], let  $w$  be the size of the considered neighborhood and  $T$  be the total number of iterations required to convergence. Then the total computational time required for this model is  $O(M * N * T * w)$ .

LIF model uses a truncated Gaussian window  $K_\sigma(x)$  with standard deviation  $\sigma$  and of size  $4k + 1$  by  $4k + 1$ , where  $k$  is the greatest integer smaller than  $\sigma$ . The convolution term  $K_\sigma(x)$  is computed only once before the iteration. However, LIF model includes two convolution terms in each iteration. The size of the regularized Gaussian kernel is truncated into an  $n \times n$  mask with  $n \leq 5$ . Thus, total computational complexity of LIF model is  $O(n^2 \times N)$ , where  $N$  is the image size [26]. The computational complexity of re-initialization is  $O(N \times N)$ .

InH\_ACN model is used here. In this model, the most time-consuming work is the calculation of  $\Omega'(p)$  for each pixel  $p$ . Suppose the width and height of an image  $I$  are  $w$  and  $h$ . Let  $M = w \times h$  and  $N = (2k + 1)^2 - 1 (k \in Z)$ , the running time of calculating all  $\Omega'(p)$  is  $O(MN)$ . Also, InH\_ACN model uses the standard gradient (also known as the steepest descent and its time complexity is  $O(M)$ . That is, each iteration calculation of InH\_ACN is  $O(M)$ . The times of iteration is much smaller than  $M$ , so the time complexity of InH\_ACN is  $O(M)$ .

Finally, in [Tables 7](#) and [8](#) we present the comparing results of the proposed model with the classical ACMs in terms of CPU time and the iteration number. It should be noted that the parameters of the RSF, LIF and LSACM models have been set based on that presented in their papers. The results of the C-V, ACM with SBGFLRS and ORACM models are obtained from their original codes. From [Tables 7](#) and [8](#), we can see that the CV, RSF, LIF and LSACM models have highest iteration numbers and CPU time among the seven models. Segmentation performances of algorithms on various medical images are represented at [Table 7](#). As it is shown, the proposed model has the best performance in both CPU time and the iteration number for five medical images. Especially, the C-V, RSF, LIF and LSACM models cannot meet the requirements of online processing for some images. It should be observed that the proposed model can also produce smooth object boundaries in addition to acceleration.

Retinal images in STARE database [57] have been used to test the algorithms. [Table 8](#) presents the computational complexity of the models for retinal images. Except [Fig. 13](#), the proposed model has the best performance. As is shown that although the ORACM has lower iteration number for [Fig. 13](#), it cannot segment right object boundaries.

**Table 8**

The comparison results for the elapsed time (s) and the number of iterations. The bolded values represent the best calculation time and iteration number.

		C-V	ACM with SBGFRLS	ORACM	RSF	LIF	LSACM	Our model
<b>Fig. 13</b>	Time	21.95	13.29	1.13	8.74	9.24	5.58	<b>0.96</b>
	Iteration	76	64	<b>9</b>	200	300	300	11
<b>Fig. 14</b>	Time	383.72	3.77	0.68	8.92	10.64	8.81	<b>0.31</b>
	Iteration	404	33	<b>6</b>	200	300	300	<b>6</b>
<b>Fig. 15</b>	Time	289.98	3.27	0.54	8.99	21.85	7.63	<b>0.24</b>
	Iteration	443	33	<b>5</b>	200	300	300	6

## 5. Conclusion

In this paper, we present a new active contour model for image segmentation. Contrary to traditional active contour models, the proposed model does not use the gradient computation. The proposed level set function is composed of eigenvalues of the Hessian matrix and a region-based SPF function. The Gaussian kernel is used by the level set smoothing term to provide the curve smooth. Extensive experiments on real images demonstrate the superiorities of the proposed method over the traditional segmentation methods, such as the C-V, ACM with SBGFRLS, ORACM, LIF, RSF and LSACM models. From the experimental results, the proposed model can provide a desirable segmentation for low contrast medical images. The developed model efficiently obtains all interior and exterior object boundaries in medical and consumer images with holes, noisy and weak edges. In addition, its computational complexity is less than the classical methods, and it has less iteration number.

It should be noted that the proposed model performs only bimodal image segmentation. It cannot detect object boundaries in color images. Up to our knowledge, color image segmentation is a difficult problem, which will be the object of further research. On the other hand, the proposed model still does not work in 3-D medical images. Considering these problems will be part of our next work. One other extension of our work is to study the use of shape priors and texture features to improve the quality of image segmentation.

## Appendix. Computational complexity analysis of the proposed model

<b>Main Function</b>		
<b>Time Cost</b>	<b>#</b>	<b>Function Steps</b>
		<b>Input:</b> $[I]_{M \times N}$ gray scaled image with size $M \times N$ , $[u]_{M \times N}$ initial contour mask image with size $M \times N$ and it consists values between $[-1, 1]$ , $\sigma$ standart variation of Gauss filter mask with size $m \times n$ .
		<b>Output:</b> $[I_{seg}]_{M \times N}$ output segmented image with size $M \times N$
O(1)	1:	$[row, col] = \text{size}(Img);$
O( $mn$ )	2:	$G = \text{fspecial('gaussian', } m, n, \sigma);$ itr=1;
O( $MN$ )	3:	$HuPos = u >= 0;$
O( $MN$ )	4:	$HuNeg = \sim HuPos;$
O( $MN$ )	5:	$diff = \text{sum}(u);$
O( $3MNmn$ )	6:	$[Dxx, Dxy, Dyy] = \text{Hessian2D}(Img, 1);$
O( $21MN$ )	7:	$[\Lambda_1, \Lambda_2] = \text{Eig2image}(Dxx, Dxy, Dyy);$
O( $4MN$ )	8:	$\mu = \sqrt{\Lambda_1^2 + \Lambda_2^2};$
	9:	<b>while</b> $abs(diff) > 0 \& itr < 50$
O( $3MN$ )	10:	$c1 = \text{sum}(Img.^* HuNeg) / \text{sum}(HuNeg);$
O( $3MN$ )	11:	$c2 = \text{sum}(Img.^* HuPos) / \text{sum}(HuPos);$
O( $3MN$ )	12:	$spf = Img - (c1 + c2)/2;$
O( $2MN$ )	13:	$spf = spf / \max(abs(spf));$
O( $MN$ )	14:	$u = spf.^* \mu;$
O( $MN$ )	15:	$HuPos = \text{Heaviside}(u, HevEps);$
O( $MN$ )	16:	$HuNeg = \sim HuPos;$
O( $MN$ )	17:	$u = HuPos - HuNeg;$
O( $MNmn$ )	18:	$u = \text{conv2}(u, G, 'same');$ itr++;
		<b>end</b>
$T(M, N, m, n) = O(50(15MN + MNmn) + 3MNmn + 21MN) \cong O(53MNmn + 771MN)$		

**Hessian2D Function**

Time Cost	#	Function Steps
		<b>Input:</b> $[I]_{M \times N}$ image with size $M \times N$ , $\sigma$ filter size ( $m = n = 2(3\sigma) + 1$ )
		<b>Output:</b> $[D_{xx}]_{M \times N}$ , $[D_{xy}]_{M \times N}$ , $[D_{yy}]_{M \times N}$ horizontal, vertical and diagonal hessian image with size $M \times N$
O( $mn$ )	1:	$[X, Y] = \text{grid}(m, n);$
O( $9mn$ )	2:	$G_{xx} = (X.^2/\sigma^2 - 1)\exp(-(X.^2 + Y.^2)/2\sigma^2)/2\pi\sigma^4;$
O( $9mn$ )	3:	$G_{xy} = (X.*Y)/(2\pi\sigma^6)\exp(-(X.^2 + Y.^2)/(2\sigma^2));$
O( $mn$ )	4:	$G_{yy} = G_{xx}';$
O( $MNmn$ )	5:	$D_{xx} = \text{imfilter}(I, G_{xx}, \text{'conv}');$
O( $MNmn$ )	6:	$D_{xy} = \text{imfilter}(I, G_{xy}, \text{'conv}');$
O( $MNmn$ )	7:	$D_{yy} = \text{imfilter}(I, G_{yy}, \text{'conv}');$

$$T(M, N, m, n) = O(3MNmn + 20mn) \cong O(3MNmn)$$

**Eig2image Function**

Time Cost	#	Function Steps
		<b>Input:</b> $[D_{xx}]_{M \times N}$ , $[D_{xy}]_{M \times N}$ , $[D_{yy}]_{M \times N}$ horizontal, vertical and diagonal Hessian image with size $M \times N$ .
		<b>Output:</b> $[\Lambda_1]_{M \times N}$ , $[\Lambda_2]_{M \times N}$ eigenvalues of the Hessian matrix with size $M \times N$
O( $6MN$ )	1:	$\text{tmp} = \sqrt{(D_{xx} - D_{yy})^2 + 4D_{xy}^2}$
O( $2MN$ )	2:	$v2x = 2D_{xy}; v2y = D_{yy} - D_{xx} + \text{tmp};$
		<b>% Calculate Eigenvalues</b>
O( $3MN$ )	3:	$\mu_1 = 0.5*(D_{xx} + D_{yy} + \text{tmp});$
O( $3MN$ )	4:	$\mu_2 = 0.5*(D_{xx} + D_{yy} - \text{tmp});$
		<b>% Sort Eigen Values and Get Eigen Image</b>
O( $3MN$ )	5:	$\text{check} = \text{abs}(\mu_1) > \text{abs}(\mu_2);$
O( $2MN$ )	6:	$\Lambda_1 = \mu_1; \Lambda_1(\text{check}) = \mu_2(\text{check});$
O( $2MN$ )	7:	$\Lambda_2 = \mu_2; \Lambda_2(\text{check}) = \mu_1(\text{check});$

$$T(M, N, m, n) = O(21MN)$$

**References**

- [1] M. Kass, A. Witkin, D. Terzopoulos, Snakes: Active contour models, Int. J. Comput. Vis. 1 (4) (1988) 321–331.
- [2] L. Cohen, On active contour models and balloons, Comput. Graph. Image Process. 53 (1991) 211–218.
- [3] C. Xu, J. Prince, Snakes, shapes, and gradient vector flow, IEEE Trans. Image Process. 10 (1998) 359–369.
- [4] C. Xu, J. Prince, Generalized gradient vector flow external forces for active contours, Signal Process. 71 (2) (1998) 131–139.
- [5] D. Ren, W. Zuo, X. Zhao, Z. Lin, D. Zhang, Fast gradient vector flow computation based on augmented Lagrangian method, Pattern Recognit. Lett. 34 (2013) 219–225.
- [6] C. Li, C.Y. Kao, J.C. Gore, Z. Ding, Minimization of region-scalable fitting energy for image segmentation, IEEE Trans. Image Process. 17 (10) (2008) 1940–1949.
- [7] K. Zhang, L. Zhang, K.M. Lam, D. Zhang, A level set approach to image segmentation with intensity inhomogeneity, IEEE Trans. Cybern. 46 (2) (2016) 546–557.
- [8] T. Chan, L. Vese, Active contours without edges, IEEE Trans. Image Process. 10 (2) (2001) 266–277.
- [9] L. Wang, L. He, A. Mishra, C. Li, Active contours driven by local Gaussian distribution fitting energy, Signal Process. 89 (12) (2009) 2435–2447.
- [10] K. Ni, X. Bresson, T. Chan, S. Esedoglu, Local histogram based segmentation using the Wasserstein distance, Int. J. Comput. Vis. (2009) 97–111.
- [11] T.F. Chan, S. Esedoglu, M. Nikolova, Algorithms for finding global minimizers of images egmentation and denoising models, SIAM J. Appl. Math. 66 (5) (2006) 1632–1648.
- [12] P. Yan, W. Zhang, B. Turkbey, P.L. Choyke, X. Li, Global structure constrained local shape prior estimation for medical image segmentation, Comput. Vis. Image Understand 117 (2013) 1017–1026.
- [13] V. Caselles, F. Catte, T. Coll, F. Dibos, A geometric model for active contours in image processing, Numer. Math. 66 (1) (1993) 1–31.
- [14] R. Malladi, J.A. Sethian, B.C. Vemuri, Shape modeling with front propagation: A level set approach, IEEE Trans. Pattern Anal. Mach. Intell. 17 (2) (1995) 158–175.
- [15] V. Caselles, R. Kimmel, G. Sapiro, Geodesic active contours, Int. J. Comput. Vis. 22 (1) (1997) 61–79.
- [16] M. Holtzman-Gazit, R. Kimmel, N. Peled, D. Goldsher, Segmentation of thin structures in volumetric medical images, IEEE Trans. Image Process. 15 (2) (2006) 354–363.
- [17] L.D. Cohen, R. Kimmel, Global minimum for active contour models: A minimal path approach, Int. J. Comput. Vis. 24 (1) (1997) 57–78.
- [18] C. Li, C. Xu, C. Gui, M.D. Fox, Distance regularized level set evolution and its application to image segmentation, IEEE Trans. Image Process. 19 (12) (2010) 3243–3254.
- [19] K. Zhang, L. Zhang, H. Song, W. Zhou, Active contours with selective local or global segmentation: A new variational approach and level set method, Image Vis. Comput. 28 (4) (2010) 668–676.
- [20] M.F. Talu, ORACM: Online region-based active contour model, Expert Syst. Appl. 40 (16) (2013) 6233–6240.
- [21] Q. Li, T. Deng, W. Xie, Active contours driven by divergence of gradient vector flow, Signal Process. 120 (2016) 185–199.

- [22] C. Li, R. Huang, Z. Ding, J.C. Gatenby, D.N. Metaxas, J.C. Gore, A level set method for image segmentation in the presence of intensity inhomogeneities with application to mri, *IEEE Trans. Image Process.* 20 (7) (2011) 2007–2016.
- [23] D. Mumford, J. Shah, Optimal approximations by piecewise smooth functions and associated variational problems, *Comm. Pure Appl. Math.* 42 (5) (1989) 577–685.
- [24] E.H.S. Diop, V. Burdin, Bi-planar image segmentation based on variational geometrical active contours with shape priors, *Med. Image Anal.* 17 (2) (2013) 165–181.
- [25] P. Rahmati, A. Adler, G. Hamarneh, Mammography segmentation with maximum likelihood active contours, *Med. Image Anal.* 16 (6) (2012) 1167–1186.
- [26] K. Zhang, H. Song, L. Zhang, Active contours driven by local image fitting energy, *Pattern Recognit.* 43 (4) (2010) 1199–1206.
- [27] N. Paragios, R. Deriche, Geodesic active regions and level set methods for supervised texture segmentation, *Int. J. Comput. Vis.* 46 (2002) 223–247.
- [28] I. Ersoy, F. Bunyak, M.A. Mackey, K. Palaniappan, Cell segmentation using Hessian-based detection and contour evolution with directional derivatives, in: 15th IEEE International Conference on Image Processing, 2008, pp. 1804–1807.
- [29] Y. Zhang, B.J. Matuszewski, L.K. Shark, C.J. Moore, medical image segmentation using new hybrid level-set method, in: Fifth International Conference BioMedical Visualization: Information Visualization in Medical and Biomedical Informatics, 2008, pp. 71–76.
- [30] Y. Shang, R. Deklerck, E. Nyssen, A. Markova, J. de Mey, X. Yang, K. Sun, Vascular active contour for vessel tree segmentation, *IEEE Trans. Biomed. Eng.* 58 (4) (2011) 1023–1032.
- [31] J. Jin, L. Yang, X. Zhang, M. Ding, Vascular tree segmentation in medical images using hessian-based multiscale filtering and level set method, *Comput. Math. Methods. Med.* 2013 (2013) Article ID 502013, 9 pages <http://dx.doi.org/10.1155/2013/502013>.
- [32] G. Doğan, Fast minimization of region-based active contours using the shape hessian of the energy, in: 5th International Conference on Scale Space and Variational Methods in Computer Vision, 2015, pp. 307–319.
- [33] Y.Q. Wang, W.F. Chen, T.L. Yu, Y.T. Zhang, Hessian based image structure adaptive gradient vector flow for parametric active contours, in: IEEE International Conference on Image Processing, 2010, pp. 649–652.
- [34] R. Su, C. Sun, T.D. Pham, Junction detection for linear structures based on hessian, correlation and shape information, *Pattern Recognit.* 45 (2012) 3695–3706.
- [35] R. Lakemond, S. Sridharan, C. Fookes, Hessian-based affine adaptation of salient local image features, *J. Math. Imaging Vis.* 44 (2012) 150–167.
- [36] E. Agu, Lecture 5: Edge detection (part 2) & corner detection, <https://web.cs.wpi.edu/~emmanuel/courses/cs545/S14/slides/lecture05.pdf>, last accessed March 06, 2017.
- [37] W. Freeman, E. Adelson, The design and use of steerable filters, *IEEE Trans. Pattern Anal. Mach. Intell.* 13 (1991) 891–906.
- [38] K. Hanbay, N. Alpaslan, M.F. Talu, D. Hanbay, A. Karci, A.F. Kocamaz, Continuous rotation invariant features for gradient-based texture classification, *Comput. Vis. Image Underst.* 132 (2015) 87–101.
- [39] J. Hladuvka, E. Gröller, Smallest second-order derivatives for efficient volume-data representation, *Comput. Graph.* 26 (2) (2002) 229–238.
- [40] J. Zhang, H. Zhao, J. Liang, Continuous rotation invariant local descriptors for texton dictionary-based texture classification, *Comput. Vis. Image Underst.* 117 (1) (2013) 56–75.
- [41] M.P. Do Carmo, *Differential Geometry of Curves and Surfaces*, Prentice-Hall, 1976.
- [42] P. Perona, J. Malik, Scale-space and edge detection using anisotropic diffusion, *IEEE Trans. Pattern Anal. Mach. Intell.* 12 (1990) 629–640.
- [43] A.F. Frangi, W.J. Niessen, K.L. Vincken, M.A. Viergever, Multiscale vessel enhancement filtering, in: Medical Image Computing & Computer Assisted Interventions, in: Lecture Notes in Computer Science, vol. 1496, 1998, pp. 130–137.
- [44] S. Gerber, T. Tasdizen, R. Whitaker, Robust non-linear dimensionality reduction using successive 1-dimensional Laplacian eigenmaps, in: Proceedings of the 24th International Conference on Machine Learning, 2007, pp. 281–288.
- [45] B. Nadler, F. Penna, R. Garello, Performance of eigenvalue-based signal detectors with known and unknown noise level, in: Proc. IEEE International Conference on Communications, ICC, Kyoto, Japan, 2011, pp. 1–5.
- [46] R. Unnikrishnan, C. Pantofaru, M. Hebert, Toward objective evaluation of image segmentation algorithms, *IEEE Trans. Pattern Anal. Mach. Intell.* 29 (6) (2007) 929–944.
- [47] M. Polak, H. Zhang, M. Pi, An evaluation metric for image segmentation of multiple objects, *Image Vis. Comput.* 27 (8) (2009) 1223–1227.
- [48] K. Hanbay, M.F. Talu, Segmentation of SAR images using improved artificial bee colony algorithm and neutrosophic set, *Appl. Soft Comput.* 21 (2014) 433–443.
- [49] W. Li, J. Yao, L. Yuan, Q. Zhou, The segmentation of the body of tongue based on the improved level set in TCM, *Lecture Notes in Comput. Sci.* 6330 (2010) 220–229.
- [50] I.E. Abdou, W.K. Pratt, Quantitative design and evaluation of enhancement/ thresholding edge detectors, *Proc. IEEE* 67 (5) (1979) 753–763.
- [51] K. Bowyer, C. Kranenburg, S. Dougherty, Edge detector evaluation using empirical roc curves, *Comput. Vis. Image Underst.* 84 (1) (2001) 77–103.
- [52] U. Kirchmaier, S. Hawe, K. Diepold, A swarm intelligence inspired algorithm for contour detection in image, *Appl. Soft Comput.* 13 (6) (2013) 3118–3129.
- [53] A. Sengur, Y. Guo, Color texture image segmentation based on neutrosophic set and wavelet transformation, *Comput. Vis. Image Underst.* 115 (8) (2011) 1134–1144.
- [54] G. Agam, I.S.G. Armato, C. Wu, Vessel tree reconstruction in thoracic CT scans with application to nodule detection, *IEEE Trans. Med. Imag.* 24 (4) (2005) 486–499.
- [55] R. Su, C. Sun, C. Zhang, T.D. Pham, A new method for linear feature and junction enhancement in 2D images based on morphological operation, oriented anisotropic Gaussian function and hessian information, *Pattern Recognit.* 47 (2014) 3193–3208.
- [56] R. Unnikrishnan, M. Hebert, Measures of similarity, in: Proc. IEEE Workshop Computer Vision Applications, 2005, 1, pp. 394–394.
- [57] A. Hoover, V. Kouznetsov, M. Goldbaum, Locating blood vessels in retinal images by piecewise threshold probing of a matched filter response, *IEEE Trans. Med. Imag.* 19 (3) (2000) 203–210.
- [58] N. Otsu, Threshold selection method from gray-level histograms, *IEEE Trans. Syst. Man, Cybern. Syst.* 9 (1) (1979) 62–66.
- [59] A. Mondal, S. Ghosh, A. Ghosh, Robust global and local fuzzy energy based active contour for image segmentation, *Appl. Soft Comput.* 47 (2016) 191–215.
- [60] L. Dai, J. Ding, J. Yang, Inhomogeneity-embedded active contour for natural image segmentation, *Pattern Recognit.* 48 (8) (2015) 2513–2529.